Materials Science & Engineering A 764 (2019) 138209

Contents lists available at ScienceDirect

Materials Science & Engineering A

journal homepage: www.elsevier.com/locate/msea

Additive manufacturing of functionally graded materials: A review

Chi Zhang[a], Fei Chen[a,*], Zhifeng Huang[a], Mingyong Jia[a], Guiyi Chen[a], Yongqiang Ye[a], Yaojun Lin[a], Wei Liu[b], Bingqing Chen[b], Qiang Shen[a], Lianmeng Zhang[a], Enrique J. Lavernia[c]

[a] State Key Lab of Advanced Technology for Materials Synthesis and Processing, Wuhan University of Technology, Wuhan, 430070, China
[b] Beijing International Aeronautical Materials Corporation, Beijing, 10080, China
[c] Department of Materials Science and Engineering, University of California, Irvine, CA, 92697, USA

ARTICLE INFO

Keywords:
Functionally graded materials
Additive manufacturing
Toolpath optimization
Microstructures
Mechanical behavior

ABSTRACT

Functionally graded materials (FGMs) represent a class of novel materials in which compositions/constituents and/or microstructures gradually change along single or multiple spatial directions, resulting in a gradual change in properties and functions which can be tailored for enhanced performance. FGMs can be fabricated using a variety of well-established processing methods; however, it is also known that there are inherent drawbacks to existing synthesis methods. As an emerging technology that provides a high degree of control over spatial resolution, additive manufacturing (AM) provides an intriguing pathway to circumvent the drawbacks of currently available methods. AM involves the selective deposition of individual layers of single or multiple materials, and as such it offers the potential of local control of composition and microstructure in multiple dimensions; such process conditions, in principle, can be tailored to construct complex FGMs with multi-dimensional and directional gradient structures. In this review paper, our current understanding of important issues, such as modeling, processing, microstructures and mechanical properties, as related to FGMs produced via AM, are described and discussed in an effort to assess the state of the art in this field as well as to provide insight into future research directions.

1. Introduction to functionally graded materials (FGMs)

When a space plane travels through the atmosphere, its combustion chamber must sustain aggressive environments as well as temperatures as high as 1000–2000 K which are so extreme that conventional composite materials are unable to meet the required performance criteria. Under such conditions, failure in a composite material occurs via delamination, during which fibers separate from the matrix [1]. To solve this problem, Naotake proposed a new class of composite materials, namely functionally graded materials (FGMs) [2], based on the observations of naturally grown materials and structures, such as bone, wood, teeth and fish scales, which consist of graded structures and as such exhibit properties that surpass those of the individual component materials [3–7]. FGMs are characterized by gradual transitions in either compositions/constituents or microstructures (e.g., grain size, texture, porosity, etc.), along at least one direction, leading to functional changes associated with at least one property [8,9]. FGMs can be classified into discontinuous and continuous, as schematically shown in Fig. 1a and b. In discontinuous FGMs, compositions and/or microstructures change in a stepwise mode usually with the presence of interface. In contrast, in continuous FGMs compositions and/or microstructures continuously changes with positions. Fig. 1c through h are schematic diagrams showing a variety of FGMs. Moreover, graded structures are present either throughout the entire material or only in some localized regions [10].

The graded structures in FGMs can effectively lower residual stress level, thereby enhancing mechanical and physical properties. In discontinuous FGMs, not only do the interfaces between layers but also the interlayer characteristics affect the magnitude of the resultant residual stress [11]. For example, the volume fraction of a specific constituent phase X at the interface of layer i, f_{X_i} as a function of the distance away from the FGM surface, y_i, can be evaluated by the following equation:

$$f_{X_i} = \left(\frac{y_i}{t}\right)^p \tag{1}$$

where t is the total height of the FGM, and p is the material exponent. The graded structure in each layer of an FGM can be optimized using Eq. (1). In related work, K. Pietrzak et al. [11] studied the residual thermal stresses in an Al_2O_3 –heat resistant steel assembly. They found that, by introducing a functionally graded (FG) structure Al_2O_3 − Cr layer between the Al_2O_3 and the steel, the residual stresses in the

* Corresponding author.
E-mail address: chenfei027@whut.edu.cn (F. Chen).

https://doi.org/10.1016/j.msea.2019.138209
Received 9 May 2019; Received in revised form 22 July 2019; Accepted 24 July 2019
Available online 29 July 2019

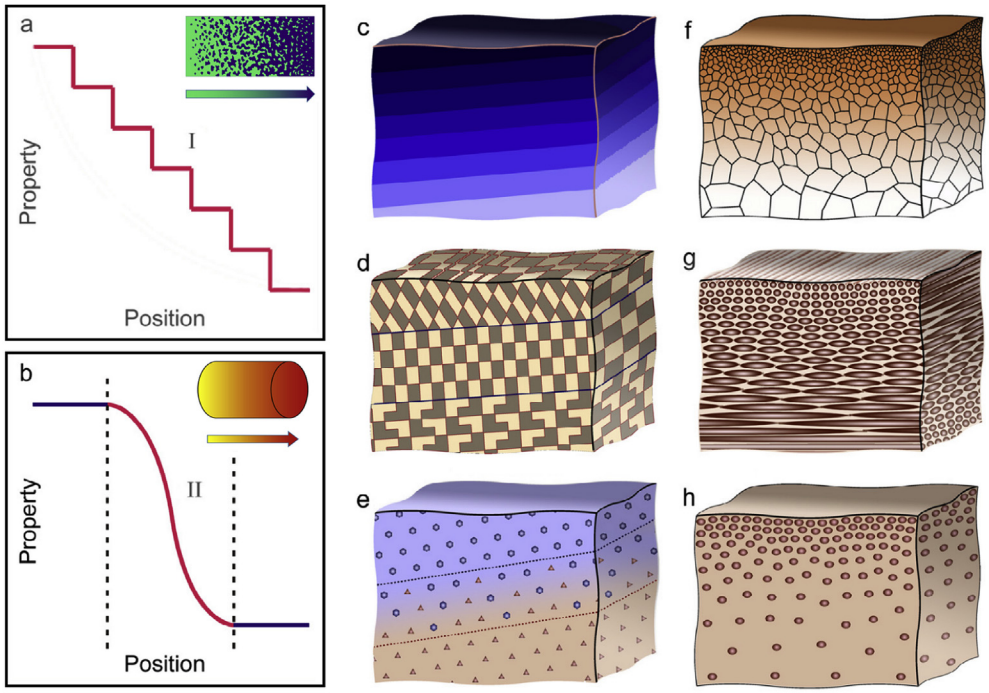

Fig. 1. Schematic diagrams illustrating: (a) discontinuous and (b) continuous FGMs, respectively. (c), (d) and (e) schematic diagrams showing discontinuous FGMs that contain interfaces with gradual change in composition, grain orientation and volume fractions of two types of second-phase particles, respectively. (f), (g) and (h) schematic diagrams showing continuous FGMs in absence of interfaces and with gradual change in grain size, fiber orientation and volume fraction of second-phase particles [10].

assembly can be reduced by about 50% [11,12].

2. Manufacturing of FGMs

2.1. Conventional manufacturing techniques for FGMs

Manufacturing techniques play a critical role in achieving the designed compositional and microstructural distribution and thus the properties of FGMs. In terms of geometry, there are two categories of FGMs: thin film/coating and bulk. The processing techniques used to synthesize thin film/coating FGMs include gas-based methods and other methods [13]. The processing techniques that can be used to manufacture bulk FGMs can be divided into liquid-phase and solid-phase approaches. The details on techniques to manufacture both thin film/coating and bulk FGMs are summarized in Table 1 [14–19].

CVD techniques using heat, plasma or light as an energy source. During CVD, the typical gases used include: bromides, hydrides, and chlorides. To attain chemical composition gradient required in FGMs, gases ratio, gas pressure, flow rate, gas type and deposition temperature are carefully controlled [14]. However, the CVD techniques are usually energy intensive and sometimes generate hazardous gases as by-products [15].

The centrifugal casting process as used for the fabrication of FGMs can be described as follows. First, the second phase (i.e., reinforcement) is added into a molten metal to form a uniform mixture. Then, by applying gravitational/centrifugal forces, a predesigned gradient in the volume fraction of the second phase is created and maintained by controlling the solidification process [20]. Despite the potential for mass production, precise control of the distribution of the second phase presents a stringent challenge. Moreover, the mechanism underlying the centrifugal method compromises the ability to manipulate the resultant microstructure since the gradient is formed through a “natural” segregation process, and thus the types of gradients that can be designed. Although the centrifugation method can produce a continuous FGMs this method is only limited to FGMs with radial gradients [21].

Starting with mixed or pre-alloyed powders, powder metallurgy (PM) techniques as applied to produce FGMs involve stacking of powders in terms of a pre-designed spatial distribution function followed by sintering to achieve full consolidation [22]. However, published results suggest that FGMs fabricated using PM techniques almost always contain a finite amount of pores which effectively degrade the thermal, mechanical, physical, wear, magnetic and corrosion properties [23]. In light of the limitations that result from using available approaches for the fabrication of FGMs, the emergence of AM methods has been received with great interest.

Table 1
Conventional manufacturing techniques for FGMs.

Category	Method	Type of FGM
Gas based method [14–17]	• Chemical vapor deposition • Physical vapor deposition • Thermal spray • Surface reaction process	Thin film/ coating
Liquid phase process [14,15]	• Centrifugal casting, • Gel-casting • Sedimentation • Tape-casting, • Slip-casting • Electrophoretic deposition • Directional solidification	Bulk
Solid phase process [14,15]	• Powder metallurgy, • Spark plasma sintering	Bulk
Other methods [14,15,18,19]	• Self-propagating high-Temperature synthesis • Plasma spraying • Electrode deposition • Ion beam assisted deposition	Thin film/ coating

2.2. Additive manufacturing processing for FGMs

AM has been proposed as an effective approach to fabricate FGMs with optimized stress profiles and excellent formability. Moreover, the discrete nature of AM provides the potential for spatial and temporal control of the microstructure such that geometrically complex components that would be very hard to fabricate using machining, for example, can be reliably manufactured with concomitant environmental benefits [21,24–28]. In a related study, Lu et al. prepared geometrically complex (i.e., gyroid, cubic lattice and Celtic knot) samples by fused deposition modeling (FDM) [29]. In the sections that follow we will

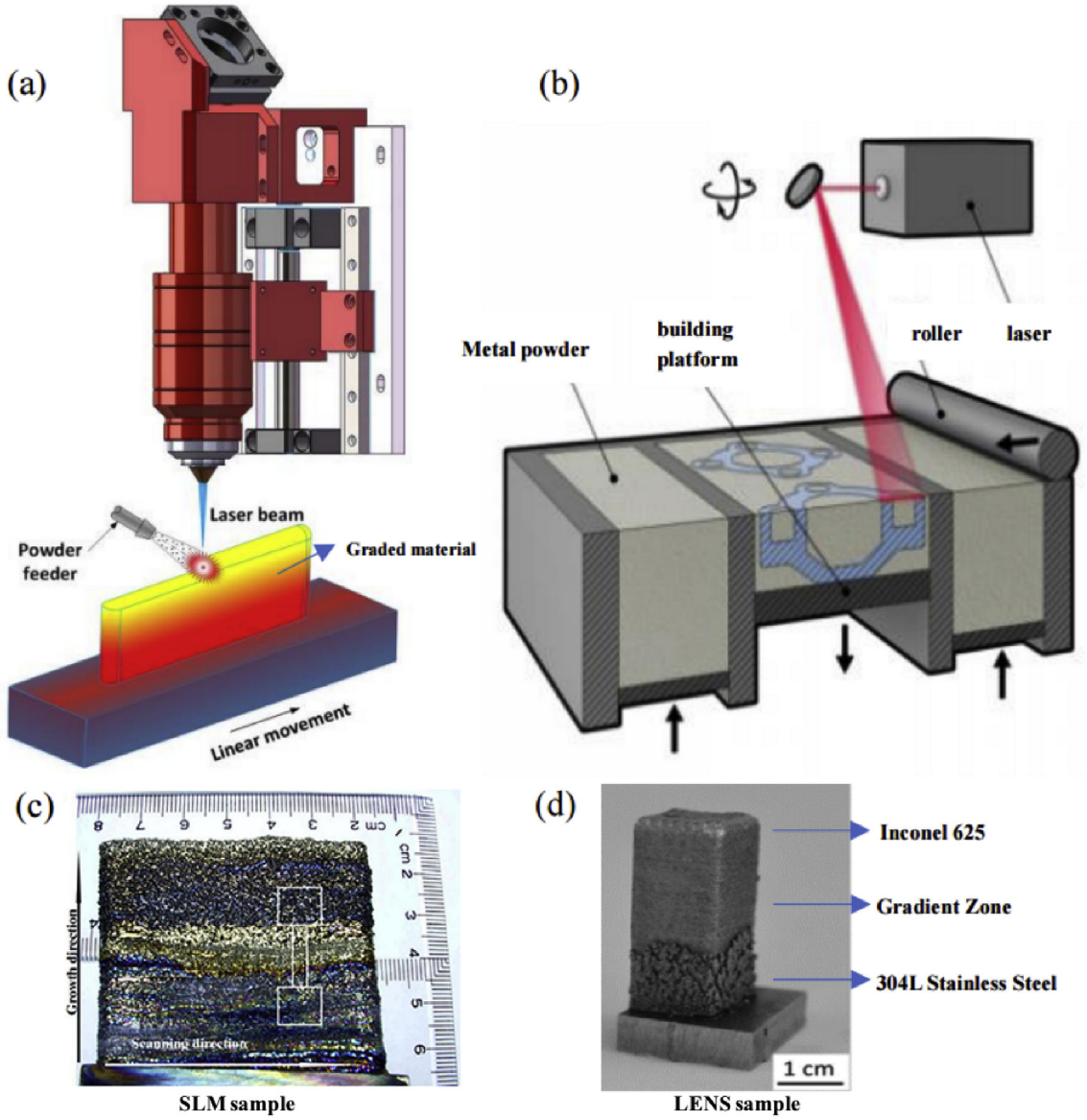

Fig. 2. Schematic diagrams showing the principles of (a) LENS [37] and (b) SLM/SLS [38], respectively. (c) FG Ti6Al4V sample fabricated by SLM [39]. (d) FG 304L stainless steel/Inconel 625 sample fabricated by LENS [40].

describe and discuss the various AM technologies that have been developed for the fabrication of FGMs.

2.2.1. Laser-based processes

Currently, there are two major laser-based AM processes, namely laser engineered net shaping (LENS) also known as directed energy deposition (DED) and selective laser sintering/melting (SLS/SLM) which are shown in Fig. 2a and b, respectively. In order to manufacture a part using a laser-based processes, the geometry of the part is first reproduced and divided into discrete layered units using computer aided design (CAD) software, and then the part is completed via layer-to-layer deposition following a predetermined sequence. Noteworthy is that molds are not required during laser-based AM processes, reducing the associated manufacturing costs. During laser-based AM processes, a layer of metal powders is rapidly heated to a melting state by high-energy laser and rapidly solidified by quenching of pre-deposited materials, as a result, the deposited parts are dense and a refined microstructure in the resultant parts can be achieved, enabling enhanced properties [30,31].

The difference between LENS and SLS/SLM is the mode used to build each individual layer. During LENS a layer is constructed by point-point deposition, i.e., powders are first directed towards a specific position followed by melting the powders by using laser heating and rapid solidification. Based on the above description, it is feasible for LENS to achieve point-to-point gradual changes in compositions/constituents by changing compositions/constituents of powders during the deposition of the part. The ability to change composition/constituent when using the point-to-point mode enables using LENS to manufacture complex FGMs with gradual composition/constituent along multiple directions and dimensions. In contrast, during SLS/SLM a layer of powders with thickness on the order of tens to thousands of micrometers are first delivered, and a laser beam selectively scans the layer of powders per a pre-determined path, melting and sintering the scanned powders. By using SLS/SLM, FGMs with a change in composition/constituent along the direction perpendicular to the layers can be readily manufactured via SLS/SLM, whereas layer-to-layer mode renders it difficult to manufacture complex FGMs with gradient composition/constituent along multiple directions and dimensions [32–36].

Val et al. [41], Choy et al. [42] and Fousová et al. [43] reported on detailed studies on the use of AM for the fabrication of FGMs. Their

results show that laser-based processes can be used to manufacture metallic FGMs parts with excellent strength, and surface roughness (< 10um) (it is important to note that values vary with machine type, material and product geometry). In addition, by using a SLM, Beal et al. [44] processed a discontinuous FGM comprising H13 stool steel and copper with weight percentages of 0%, 25% and 50% [44]. As shown in Fig. 2c and d, FGMs containing a gradient volume fraction of a secondary phase can be effectively manufactured using laser-based processes [39,40].

2.2.2. Stereolithography process

As the earliest practical rapid prototyping technology, stereolithography (SLA) has been widely used in various industry sectors such as: aviation, automotive, electric appliances, consumer goods, medical devices, to name a few, partly as a result of its ability to provide process automation combined with good surface quality and dimensional accuracy. The principle of SLA can be described as follows [45–47]: a laser with a specific wavelength (e.g., 250–300 nm) is focused on a point on the surface of a photocurable material (e.g., liquid photosensitive resin) to promote polymerization, and then moved to another point following a pre-determined sequence, doing the same operation until polymerization is completed on a layer; the part is vertically lifted by the preset height, and the aforementioned operation is repeated until the entire part is manufactured, as shown in Fig. 3a.

SLA has been broadly used to process FGMs. For example, Liu et al. [48] used topology optimization and SLA to produce FG porous materials as shown in Fig. 3b. In related work, Gonzalez et al. [49] prepared a FG semi-maxillary-like implant structure consisting of a dense outer shell and a porous bone-like central core using SLA In the FG structure, the gradient change in volume fractions of alumina and polymer [49] enables the functional characteristics of the outer shell and central core.

2.2.3. Material jetting process

The material jetting process starts with Polyjet printing, which is a powerful 3D printing technology that can produce parts from a wide range of polymers with microscopically smooth surfaces and accurate dimensions down to 0.1 mm [50]. As a result, this process can produce thin walls and complex geometries. As shown in Fig. 4a, Polyjet printing uses an array of print-heads that move along the X and Y directions during operation. The print-heads spray photopolymerizable material onto a table, the roller smoothens the surface of the sprayed materials, and the ultraviolet (UV) lamp cures the material. After the jet printing and curing of one layer is completed, the table drops by the thickness with a high degree of accuracy. The print-heads continue to spray the photosensitive polymer material for printing and curing of the next layer. The steps are repeated until the entire part is built. Usually, following Polyjet printing an additional curing process is required to modify the surface quality of the parts. The above jet process can also be used to fabricate metal parts, where subsequent sintering is required to promote metallurgical bonding between powders [50–52]. Since the type and amount of materials sprayed by print-heads are readily and flexibly adjusted, this process can be used to engineer complex FGMs with gradient compositions along multiple directions.

However, there is significant material waste using this process: materials used to make the substrate and those removed during cleaning of the nozzle are discarded [51]. Usually, materials including FGMs manufactured by this process contain more flaws than those in materials processed by other processes. In Fig. 4b, TiC/steel FGMs processed by material jetting technique is shown [53].

2.2.4. Fused deposition modelling

The principle of FDM process shown in Fig. 5a can be described as follows: a filamentous material is melted and selectively deposited by a three-dimensional sprinkler controlled computer, forming a layer with a pre-designed cross-section and cooled rapidly; then, the deposited layer drops by a height of a layer and the next layer is deposited until the entire part is manufactured [54,55]. As shown in Fig. 5b, Leu et al. [56] developed a triple extrusion method to control the compositional gradient required for paste extrusion. A limestone ($CaCO_3$) part with a graded color can be fabricated using FDM, as shown in Fig. 5c. A green part with graded composition of alumina (Al_2O_3) and zirconia (ZrO_2) was also manufactured. In related work by Singh et al. [57] Al/Al_2O_3 FGMs were prepared using a method that combines FDM with investment casting (IC).

The FDM process is a popular AM technology that provides prototyping advantages and has been widely used. FDM is a lower cost AM method that uses less expensive materials and poses no risk of toxic gases and chemical contamination. However, after FDM printing, the surface is rough and thus requires additional steps. The highest precision achievable thus far is only 0.1 mm [57]. Due to the mechanical movement of the nozzle, a support table is also required as speed is slow [58]. The characteristics of the various techniques discussed are summarized in Table 2 [59,60].

3. Toolpath planning and optimization of AM techniques for FGMs

Various contemporary AM technologies have been discussed in the previous section. There are inherent advantages and disadvantages to each of them, and there are also limitations in terms of the types of materials that these technologies can accommodate. Despite the obvious differences in terms of the process parameters that govern these distinct technologies, the selected toolpath is particularly critical as it directly influences the resultant material characteristics. An efficient toolpath strategy is able to improve precision, quality, strength as well

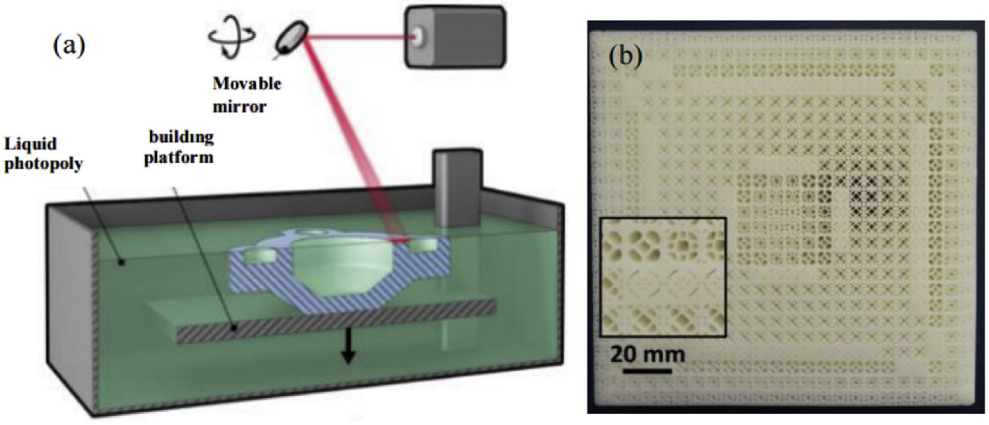

Fig. 3. Schematic diagrams showing the principles of (a) SLA [38], and (b) a FGM, specifically a cellular panel with gradient porosity made by SLA technology [48].

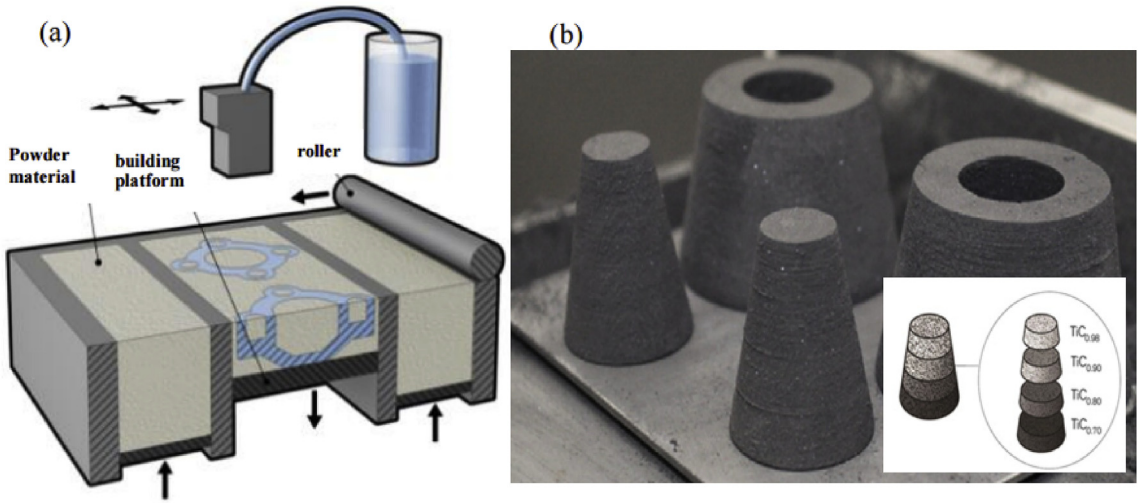

Fig. 4. Schematic diagrams showing the principles of (a) material jetting process [38], and (b) TiC/steel FGMs processed by material jetting process [53].

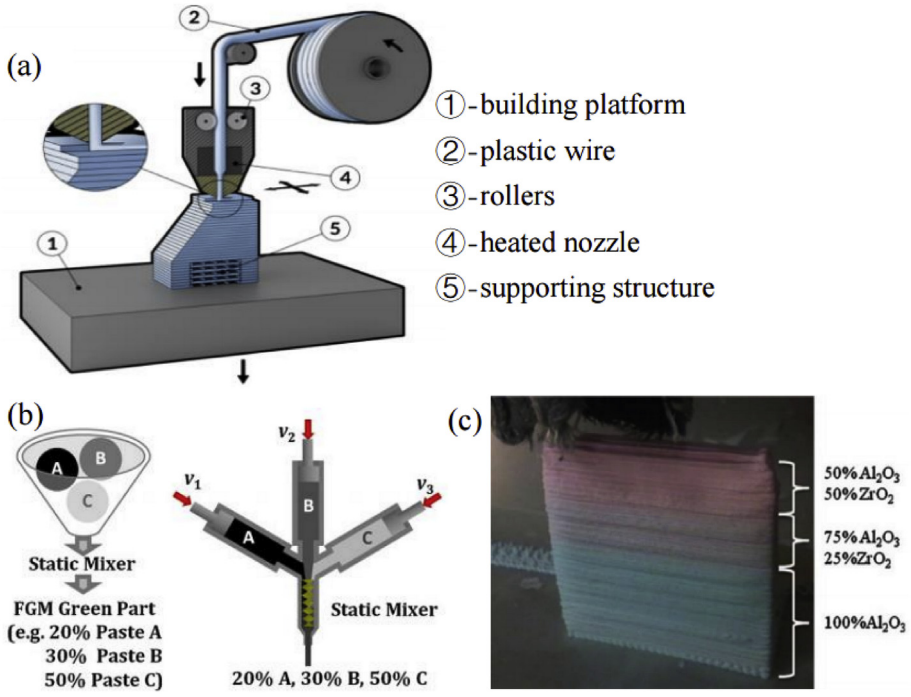

Fig. 5. (a) Schematic diagram showing the principles of FDM [38] and (b) of triple-extruder mechanism design [56]. (c) A FGM consisting of Al_2O_3 and ZrO_2 prepared by FDM [56].

as reduce building time [61]. The modeling of toolpath strategies has thus evolved as an area of interest for AM FGMs, and review of the published literature shows interesting results, as discussed in the sections that follow.

3.1. Toolpath planning and optimization

Langrana et al. [62] proposed one of the first material representation approaches as well as product design cycles for multi-material AM. The representation approach separated the geometric information of two materials while retaining the spatial relationships and sliced them into two-dimensional (2D) images appropriate for layered manufacturing. An FDM program first processed these individual building files extracted from sliced 2D images. A virtual simulation then computed the defects and voids for a given toolpath. Provided that an acceptable toolpath was generated, a sample would be built by following the toolpath while a video borescope recorded the building materials in real time. When unanticipated defects are identified using a visual feedback, the simulation assumptions are updated to provide more accurate toolpath assessments [62]. Fig. 6a illustrates the iterative process of optimizing multi-material fabrication, Fig. 6b and c shows the simulation results and the corresponding fabricated sample, respectively. In their follow up research, two intelligent features were added to the iterative toolpath generation process, which minimize the number of paths and the distance from an end point to the next starting point. In addition, an offset has been introduced between the interface of two discrete materials to eliminate the voids that may evolve from mismatch. Using this approach, bi-material prototypes devoid of inefficient toolpaths and voids were produced [63]. To manufacture a sample that is completely defect-free, however, requires changing the feedstock rate and minimizing the generation of corners to avoid deposit overfills and underfills [64], which was achieved in the work on

Table 2
Characteristics of various AM techniques [35,45,50,55,57–60].

Technology	Materials	Advantages	Disadvantages	Surface roughness
Laser-based process	• Metals • Hybrid	• High quality parts • Excellent for repair applications • Fast build process	• Balance between surface quality and speed • Limited raw materials	Less than 10 μm
SLA process	• Polymers • Ceramics • Composites	• Large parts • Excellent accuracy • Excellent surface finish and details	• Poor mechanical properties of samples • High cost • Slow building process	10 μm–100 μm
Material jetting process	• Polymers • Ceramics • Composites • Hybrid • Metals	• Various raw materials • Low waste • Low cost	• Support material is required • More wastes • Post process needed	Around 0.1 mm
FDM process	• Polymers • Composites	• Widespread use • Low cost • Ability to build ready-to-use product	• Vertical anisotropy • Slow building process • Rough surface	Around 0.1 mm

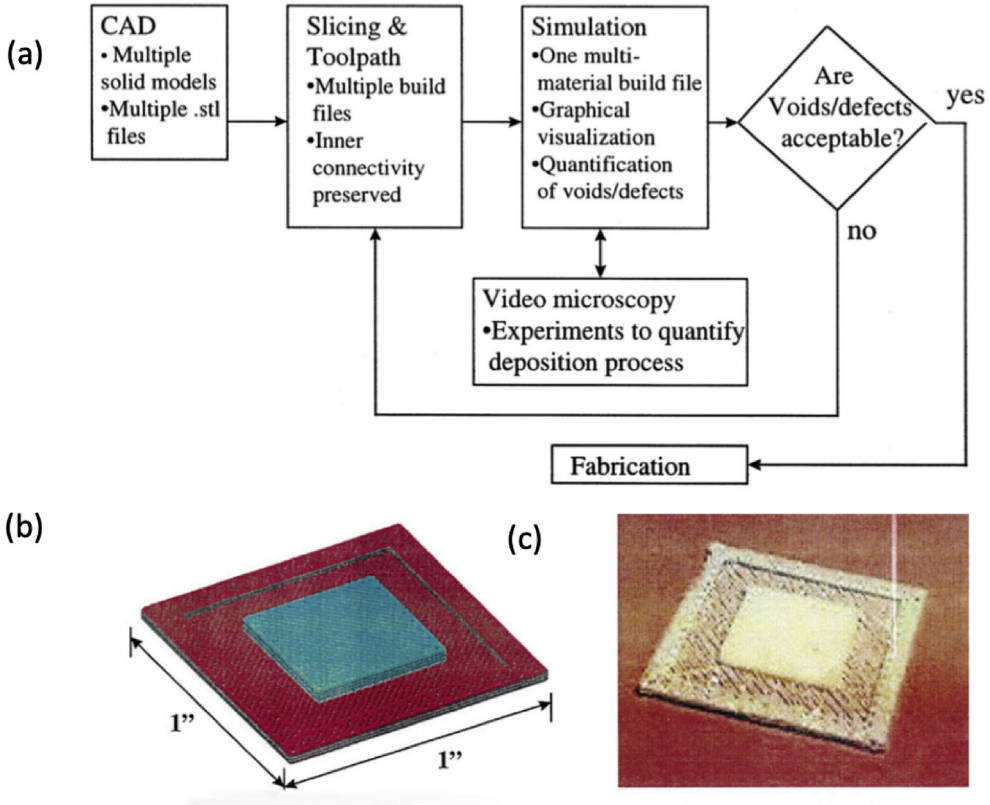

Fig. 6. (a) Design cycle of AM multi-materials from CAD to fabrication with video microscopy and simulation feedback loop. (b) virtual AM simulation of bi-material sample, and (c) fabricated bi-material sample [65].

contour-parallel toolpath optimization of Jin et al. [65].

As a result of advances in the science and technology of AM today it is possible to simultaneously deposit different materials with spatially designed distribution of microstructures (including phases, particles and chemistries) and with properties that are optimized for specific applications. However, an additional challenge that emerges during the fabrication of microstructurally graded FGMs is the representation of material information in relation to the geometry [66]. Different representation models have been proposed to resolve this problem [24,67–73], but practical implementation of these into AM programs has been challenging [74]. In related work, Zhou et al. [75] modelled the toolpath of an FGM object by assigning material functions to reference features in the B-rep geometry. The continuous material composition change was then discretized and sliced into 2D layers. This work illustrates how FGM representation can be applied to toolpath planning.

3.2. Applications of toolpath strategies

The toolpath strategies described in the previous section of this review article are rarely cited or applied in actual experimental studies. This is understandable, as the focus of most current studies remains on characterizing and analyzing the morphologies that can be attained in different AM FGMs. In related studies, Muller et al. [76,77] simulated the performance of various toolpath strategies and compared the simulation results with fabricated samples. The approach used in this particular study is described as follows. First, a comprehensive model of the entire manufacturing process was formulated. The FGM compositions were described as a function in R^3 domain, which would be printed as individual curves containing detailed information of the orientation, height and width of each deposition. Then a numerical control program is used to operate the actual manufacturing process. The complete modeling of the process enables reduction of error between

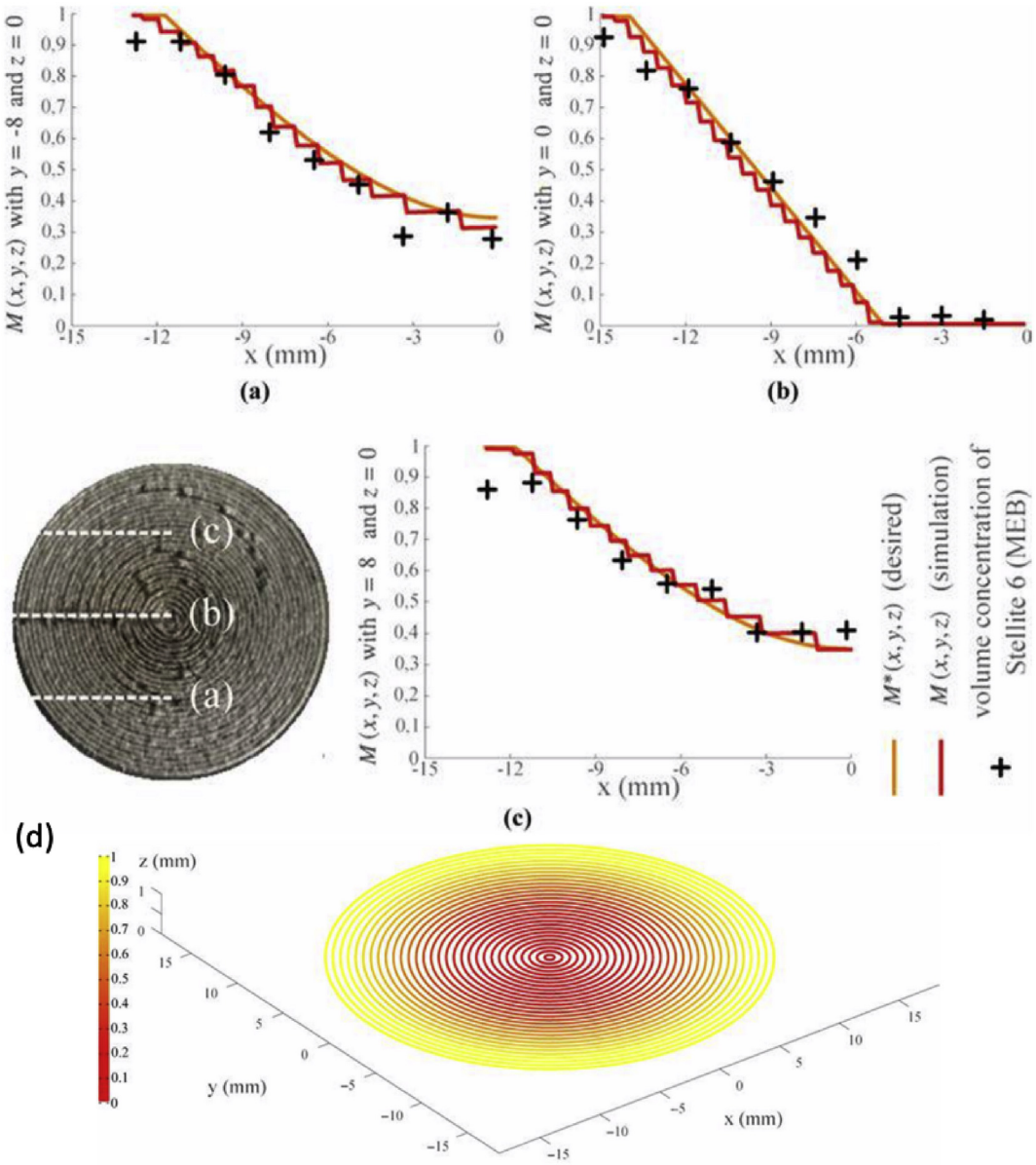

Fig. 7. (a), (b) and (c) Comparison between desired, simulated and experimental compositions in different sections, and (d) illustration for spiral contour toolpath [77].

designed composition and feed system delay [76]. A follow up study utilized predictive process control to reduce the feed delay for more accurate builds. Path strategies with large fluctuations of composition, however, still show a high degree of inaccuracy even when using a predictive control scheme. For example, two FG 316L/Stellite 6 specimens with radial compositional gradients were laser melted using a zigzag parallel strategy and a spiral contour strategy [77]. Simulations and elemental analysis were generated to be compared with the desired composition. By using the zigzag toolpath, the delay in changing feedstocks in both the experimental and simulated samples creates an almost uniform composition. Given more gradual changes in compositions by using the spiral toolpath as shown in Fig. 7a through d, the simulated and the actual compositions of the specimen much more approach the desired one than those obtained by using zigzag strategy with constant compositional changes [77].

Inspired by Muller's work [76,77], Xiao and Joshi invented an automatic toolpath generation scheme to be used in the fabrication of FGMs using AM [74]. The proposed algorithm prioritizes the scanning of neighbouring pixels with the same material composition as the previous one. When no immediate neighbour carries the same material information, the toolpath seeks the next starting point that requires the least travel time. By selecting these appropriate hierarchical rules, the optimal path could be generated for the path with the best accuracy vs. run time. Although no experimental results were reported, the simulations have taken the laser traveling speed, deposit width and layer thickness of contemporary LENS and DED systems into consideration [74].

In principle, the above described strategies, when properly implemented, should be able to improve product quality as well as reduce time and thereby costs of AM FGMs. At present, however, these strategies, unfortunately, do not seem to have direct application to the fabrication of FGMs. In the case of those AM experiments that produced parts with simplistic geometries and with linear compositional changes along the building direction, the toolpath strategies for optimization of multi-materials become in turn less useful. Factors that influence single material AM processes, however, have been used more deliberately. For laser-based processes such as SLM, the thermal history during manufacturing can result in thermal stress build-up [78] and balling

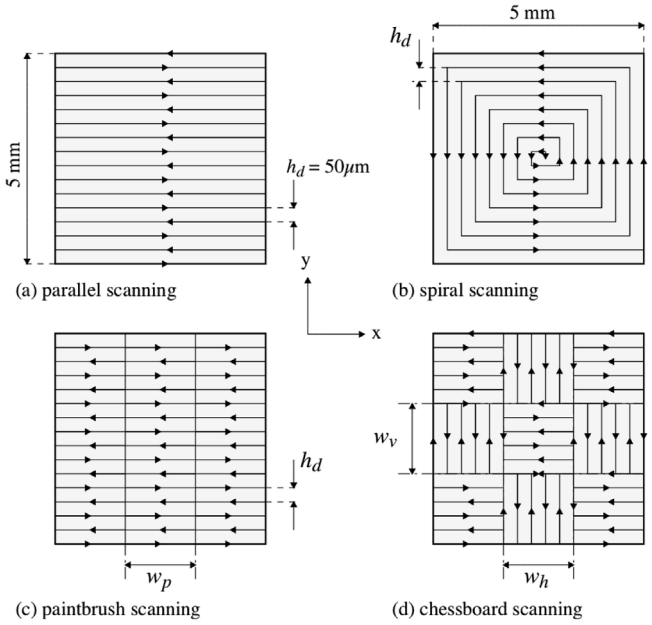

Fig. 8. Schematic diagram showing: (a) parallel scanning strategy, (b) spiral scanning, (c) paintbrush scanning, (d) chessboard scanning strategies [80].

phenomenon [79]. Jhabvala et al. [80] attempted to tackle these known issues via the selection of a proper toolpath strategy. Accordingly, parallel, spiral, paintbrush and chessboard patterns were studied. The illustration and dimensions of these four path strategies are shown in Fig. 8.

Generally, the parallel strategy causes cracking and balling in the samples, resulting from overheating or formation of thermal stresses. The scanning direction is perpendicular to the temperature gradient, which results in heterogeneous shrinkage and the formation of residual stresses. The spiral strategy can reduce the stress and heat build-up at high laser power and scanning speed, although overheating still occurs at the center of the samples. Portioning and scaling down of the scanning area has been proposed as a potential solution. Since the areas are reduced for a single scanning pattern, the accumulation of thermal defects is reduced, and it becomes easier to maintain temperature homogeneity [80]. This reduction of area approach has not been applied to SLM fabrication of homogenous materials such as Ti/Ta alloys [81]. It has however, been used for the fabrication of FGMs such as DED of ferritic/austenitic steel [82]. The residual stress mapping constructed using a contour method reveals a low and constant level of residual stress in the sample that was prepared using a chessboard scan pattern [82].

4. State of the art systems

4.1. Ti-based materials

Titanium alloys are widely used, in part due to their high strength to weight ratio, low density, and excellent corrosion resistance. In particular, Ti6Al4V is popular in aerospace applications as a result of its high strength at extreme temperatures [83–85]. Not surprisingly, several studies have been published examining the feasibility of fabricating Ti-based FGMs using AM methods. In the sections that follow we discuss key findings from these studies.

4.1.1. Ti6Al4V/TiC

Despite their attractive elevated temperature strength, Ti6Al4V alloys do suffer from poor wear resistance and low hardness, which tend to limit their applicability in the aerospace field. To address this drawback, TiC additions have been proposed as a potential solution to improve the mechanical, physical and tribological properties of Ti6Al4V alloys partly because TiC has a similar coefficient of thermal expansion, and a high hardness and moreover, is thermodynamically stable in a Ti matrix [86–92]. In related work, Li et al. [93] fabricated a FG Ti6Al4V/TiC composite (TiC volume fraction ranging from 0 vol% to 50 vol%) using a laser melting deposition (LMD) technique. Fig. 9 shows that the phases of the FGM mainly consists of αTi, β-Ti and TiC; the blocky TiC is unmelted TiC particles in the sample. It is evident that the eutectic TiC phase forms in the case of 5 vol% TiC, whereas the dendritic TiC phase appears when TiC volume fraction exceeds 10 vol%

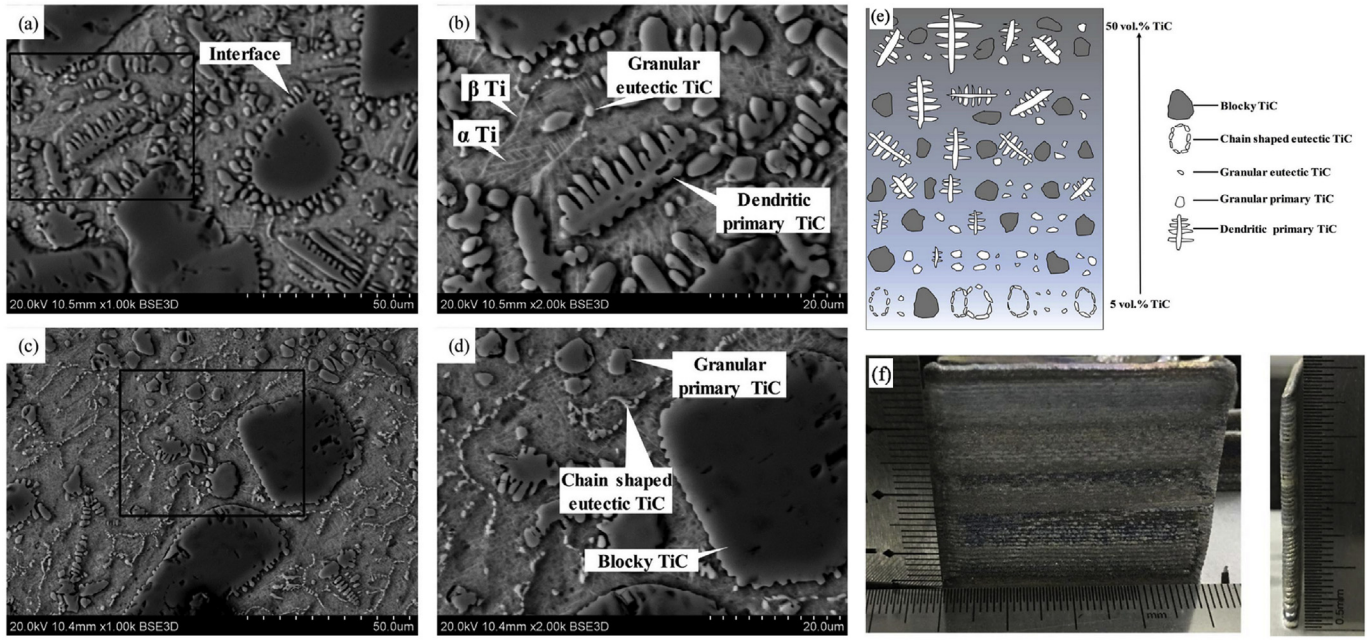

Fig. 9. Microstructure of the FGM Ti6Al4V/TiC for different locations: (a) top location, (b) higher magnification micrograph of (a), (c) middle location, (d) higher magnification micrograph of (c), (e) schematic diagram showing microstructure of FG Ti6Al4V/TiC composite, and (f) photograph of the FG Ti6Al4V/TiC composite [93].

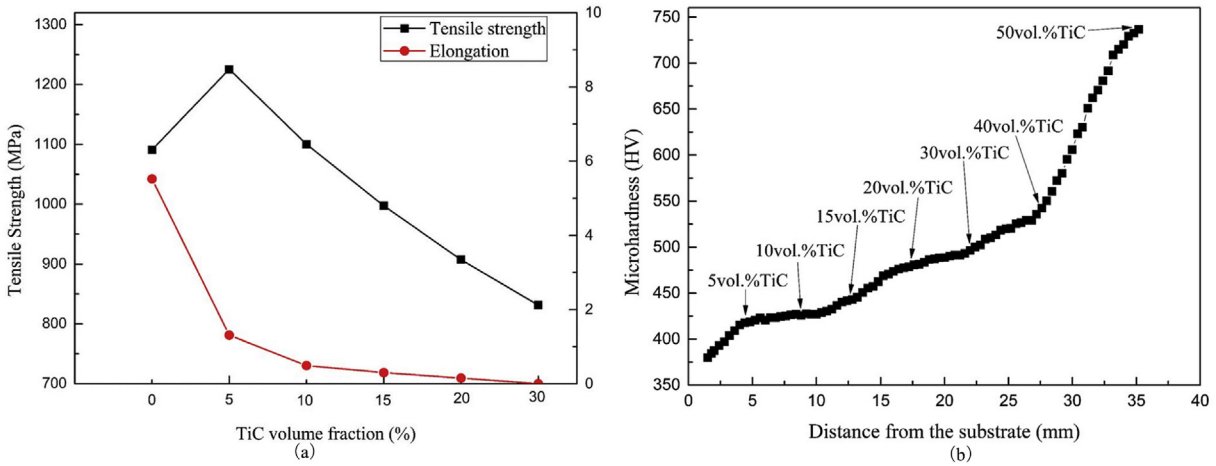

Fig. 10. (a) Tensile properties of FG Ti6Al4V/TiC composite as a function of volume fraction of TiC and (b) Vickers hardness as a function of the distance from the substrate, as well as of volume fraction of TiC [93].

[93]. Moreover, the morphology of the TiC reinforcements gradually changes from eutectic to dendritic. Since primary TiC (consists of granular TiC and dendritic TiC) will precipitate first when the TiC volume fraction exceeds 10% as carbon concentration increases and exceeds the eutectic point. Dendritic TiC with larger size will lead to premature damage of the material, limiting an improvement in its mechanical performance.

Fig. 10a shows tensile strength values as a function of volume fraction of TiC, and Vickers hardness as a function of the distance from the substrate, as well as of volume fraction of TiC. It is apparent that 5 vol% of TiC in the FG Ti6Al4V/TiC composite can improve both tensile strength and hardness. However, the tensile strength dramatically decreased when TiC exceeded 5 vol%. This degradation in mechanical properties with increasing volume fraction of TiC was attributed to an increase in the number density of unmelted and dendritic TiC particles in the sample. In contrast, as shown in Fig. 10b, the hardness increased with increasing volume fraction of TiC, ranging from 380 HV near the substrate to 737 HV in top layer, with 50 vol% TiC [93].

Other studies on FG Ti6Al4V/TiC composites reveal similar trends, both in terms of the microstructures as well as mechanical behavior [94–97]. These results are consistent with the fact when process parameters (e.g., laser power) are kept constant increasing the volume fraction of TiC invariably leads to the formation of unmelted and dendritic TiC phases, which effectively facilitate crack formation and early fracture [98–101]. Other investigators studied the influence of process parameters on the microstructure and performance of FG Ti6Al4V/TiC composites. For example, Mahamood et al. [102] used a modeling approach to simulate the influence of optimized process parameters (such as laser power, scanning speed, etc.) on different graded structures during fabrication. Two distinct materials (FG Ti6Al4V/TiC composites with TiC volume fraction ranging from 0 vol% to 50 vol%) were fabricated in this study. The sample fabricated with the optimized process parameters exhibits the higher hardness 1200 HV and better wear-resistance compared to the one with the fixed process parameters. Fewer unmelted TiC are formed in the sample fabricated with the optimized process parameters. In addition, the hardness and the wear resistance performance were also reported to increase with increasing scanning speed. However, the surface roughness increases when scanning speed exceed 0.085 m/s due to inadequate interaction between the laser and unmelted powders [103,104]. Other research by Mahamood et al. [105–107] confirmed the finding that optimized process parameters for each layer of FGMs during fabrication will improve mechanical behavior.

The size of the TiC particle will also play an important role in the mechanical properties of the FG Ti6Al4V/TiC composites. In a related study by Wang et al. [108], Ti6Al4V/TiC FGMs were prepared by using TiC particles with different size. Four types of TiC powders were used in the study: coated powders (TiC < 10 μm), and uncoated small-sized (TiC: 25–45 μm), medium-sized (TiC: 45–75 μm) and large-sized (TiC: 75–100 μm). The Ti6Al4V and TiC powders were premixed due to their irregular morphology of the TiC powders. As evident from Fig. 11a–d, no unmelted TiC are found in the FGMs fabricated using coated powders. The results are consistent with Fig. 11q since the sample fabricated with coated powders shows the best tensile results. It can be seen from Fig. 11e-p, with increasing powder size, the quantity of unmelted TiC powders increases constantly. Thus, cracks and rough interfaces are introduced into the FGMs which degrade its mechanical performance. In addition, the samples produced using coated powders exhibit far higher tensile strength (e.g., 1231.3 MPa) and elongation (e.g., 2.12%) as compared to those of the other three [108]. These results confirm that the presence of large-sized unmelted TiC powders degrades tensile strength [109,110].

In other related work, Liu et al. [111] studied how the extent of melting of the reinforcing TiC particles influences both this microstructure and the mechanical behavior of FG Ti6Al4V/TiC composites. In this study, the maximum degree of melting was defined as the complete melting of all TiC particles, whereas the least degree of melting was defined as the onset of TiC melting, as shown in the inset of Fig. 12. The laser power was adjusted from 200W to 400W to promote different degrees of TiC melting. By controlling laser power density, no dendritic phase can be found in FG Ti6Al4V/TiC with 0 vol% to 15 vol% of TiC. The formation of TiC dendritic phase cannot be avoided when volume fraction of TiC exceeds 15 vol% in premixed powders even with higher laser power density. From Fig. 12, when volume fraction of TiC is 1 vol%, a high degree of TiC melting leads to increases in both yield and ultimate strength values. No unmelted TiC particles or other detrimental phases can be detected under this condition. In the case of the composition corresponding to 5 vol% TiC, the presence of unmelted TiC particles leads to embrittlement of the deposited materials. In addition, the mechanical behavior corresponding to 10L–15L confirms the embrittlement caused by TiC particles [111].

Noteworthy is a study by Wang et al. [112], where TiB was used as reinforcement phase when manufacturing FG Ti6Al4V composites, instead of TiC. The experimental results reveal an enhanced hardness relative to that using TiC as reinforcement phase. Moreover, the wear resistance has been improved significantly due to complete dissolution of B in the matrix.

4.1.2. Ti6Al4V/stainless steel

In the nuclear and aerospace industries there is a critical need for

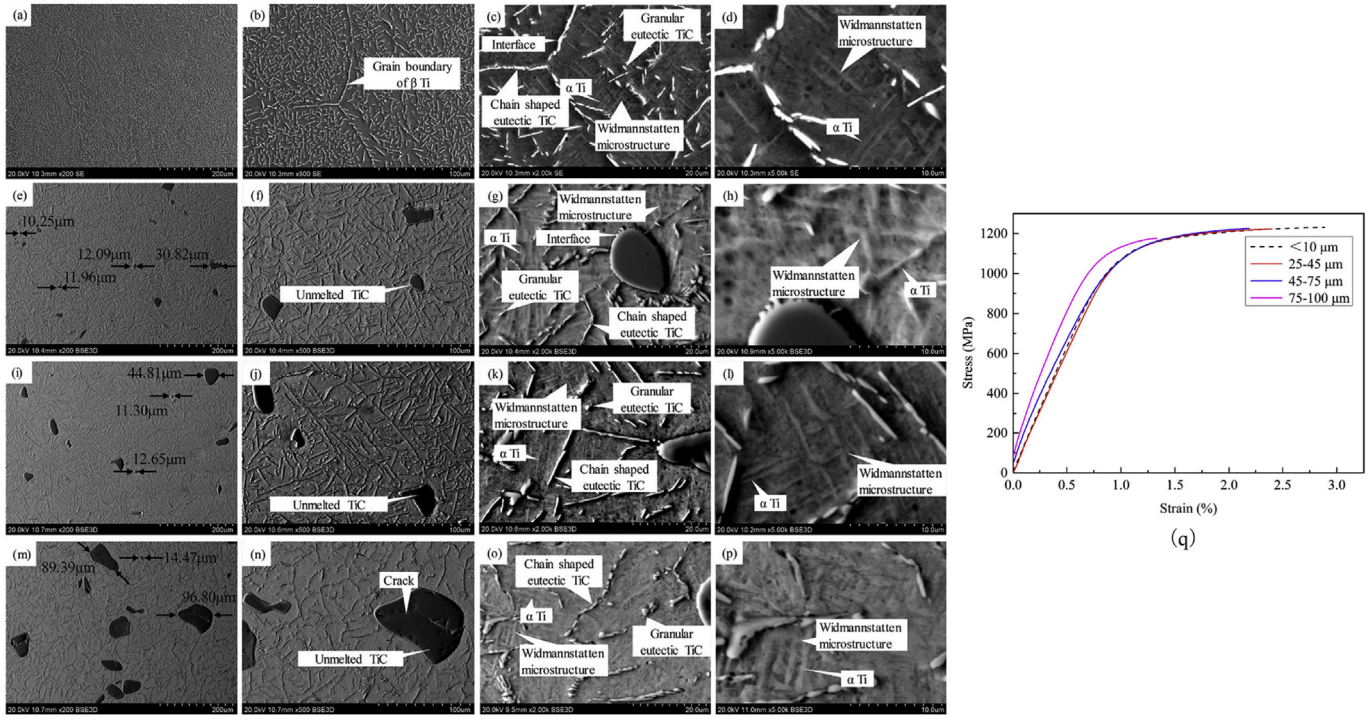

Fig. 11. Microstructure of FG Ti6Al4V/TiC composites with different TiC size: (a), (b), (c) and (d) coated powders (TiC < 10 μm); (e), (f), (g) and (h) uncoated small-sized powders (TiC: 25–45 μm); (i), (j), (k) and (l) uncoated medium-sized powders (TiC: 45–75 μm); (m), (n), (o) and (p) uncoated large-sized mixed powders (TiC: 75–100 μm); (q) tensile stress vs. strain curves of FG Ti6Al4V/TiC composites with different TiC sizes [108].

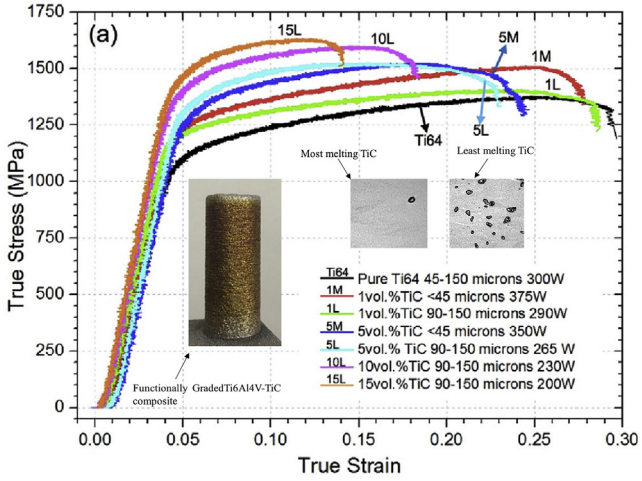

Fig. 12. Compression test results of FG Ti6Al4V/TiC composites fabricated under a series of processing parameters, where "M" and "L" denote the most and least melting control conditions of the TiC particles [111].

fabricating high-integrity joints between Ti-alloys and stainless steels [113]. These two materials are preferred because of their high strength-to-weight ratio, light weight and superior heat resistance [114]. However, the direct joining of these two types of materials poses stringent challenges. For example, traditional welding methods, such as diffusion bonding and roll bonding, can lead to the formation of brittle intermetallic compounds such as FeTi and Fe_2Ti. These intermetallic compounds will lead to the formation of unexpected residual stresses, effectively embrittling the joints and causing premature fracture [115–117]. In addition, the differences in the coefficient of thermal expansion between these two classes of materials can also lead to premature yielding and in extreme cases, interfacial delamination [118]. Not surprisingly, FGMs have been proposed as a potential solution to create a transitional interface that can avoid localized effects from the property differential between two materials. As such, Cu, Ni, Al and their alloys have been widely proposed as potential interlayer materials [119–123]. The mechanism of interlayer materials selection depends on the propensity for intermetallic phase formation between the selected interlayer material and the Ti and stainless steel alloys [124]. For example, in a study by Tomashchuk et al. [119], V was proposed as an interlayer material in an effort to avoid the formation of brittle intermetallic phases. However, the sample of 316L SS/Ti6Al4V with V as the interlayer cracked during tensile testing. Embrittlement was attributed to the presence of (Cr, V) solid solution and FeTi in the welded zone between Ti6Al4V and V. Although the solid solution is generally ductile, the ensuing embrittlement behavior can be explained by the fact that the ductile-to-brittle temperature of vanadium alloys exceeds ambient temperature.

In another study, Bobbio et al. [125] synthesized a FGM consisting of Ti6Al4V and stainless steel (SS) 304L with an intermediate layer of V. The fabrication process was performed in an argon atmosphere with a laser power operated at 600 W and a scanning speed of 12.7 mm/s by LENS. The powders used in this experiment consisted of pre-alloyed Ti6Al4V powders with diameters ranging from 44 to 177 μm, pre-alloyed SS 304L powders with sizes ranging from 45 μm to 105 μm, and V powders with sizes ranging from 45 μm to 250 μm. During fabrication, the first 28 layers of 100 vol% Ti6Al4V were first deposited on Ti6Al4V substrate successively followed by 27 layers of 75 vol% Ti6Al4V plus 25 vol% V, 26 layers of 50 vol% Ti6Al4V plus 50 vol% V, 27 layers of 25 vol% Ti6Al4V plus 75 vol% V, 27 layers of 25 vol% SS 304L plus 75 vol% V, and 7 layers of 50 vol% SS 304L plus 50 vol% V. The deposition sequence is schematically shown in Fig. 13a. In Fig. 13b, the first crack occurred at layer number 109 where the composition is 25 vol% SS304L plus 75 vol% V [125]. It was argued that this crack originated at Ti/Fe intermetallic phases because of the direct contact between Ti6Al4V and SS 304L in this transition region. A second crack formed in layer number 136 where the composition is 25 vol% SS 304L plus 75 vol% V transitioning to 50 vol% SS 304L plus 50 vol% V. A large

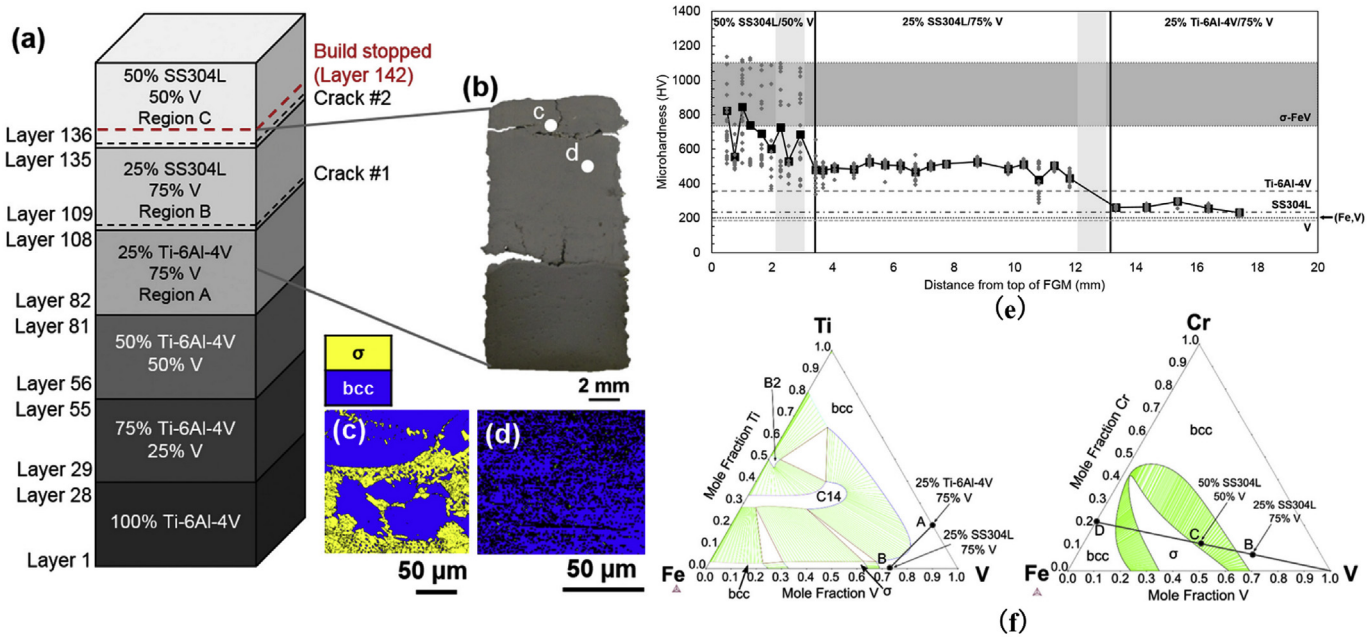

Fig. 13. (a) The schematic diagram showing the LENS process of the FGM consisting Ti6Al4V and SS 304L with an intermediate layer; (b) macrograph of the cross-section of the AM sample; (c) and (d) EBSD phase mapping in regions consisting of 50 vol% SS 304L plus 50 vol% V, and 25 vol% SS 304L plus 75 vol% V, corresponding to c and d in (b), respectively; (e) microhardness as a function of position from the top consisting of 50 vol% SS 304L plus 50 vol% V where regions containing cracks are denoted by light gray shading, the hardness values of pure σ-FeV, Ti6Al4V, 304L SS, and V, are noted by dashed lines, and the range of hardness of (Fe, V) solid solution is noted by the shaded dark gray region; (f) ternary phase diagrams used to predict the Fe–Ti–V system and the Fe–Cr–V system, with the studied graded compositions labeled as A and B in the Fe–Ti–V system, and B, C and D in the Fe–Cr–V system (regions from Fig. 13(a)) [125].

crack was generated in layer number 142 after only 7 layers of deposition of 50 vol% SS 304L plus 50 vol% V, due to the formation of the σ-FeV phase. This suggestion was validated using EBSD results, as shown in Fig. 13c, where two types of phases, namely: σ-FeV and a body-centered cubic (BCC) (Fe, V) solid solution, are evident [125]. Following the presence formation of the large crack, the experiment was discontinued. The sample was polished in order to conduct hardness measurements, which are shown in Fig. 13e. The measurements started from the top of the sample with the composition 50 vol% SS 304L plus 50 vol% V to the position corresponding to the composition of 25 vol% Ti6Al4V plus 75 vol% V. A high hardness value of 713 ± 220 HV was measured in the region with 50 vol% SS 304L plus 50 vol% V and far from the large crack, due to the formation of the σ-FeV phase. However, the region with 50 vol% SS 304L plus 50 vol% V and near the large crack exhibited an average hardness of 670 ± 240. Moreover, in this study, the method of the calculation of phase diagrams, namely CALPHAD [126–128], was implemented to design the appropriate compositions of the above graded system assuming isothermal conditions in order to avoid the formation of detrimental phases. The AM process is inherently non-equilibrium, given the repeated thermal cycling and rapid solidification experienced by each layer; however, in order to render the problem tractable, the authors assumed equilibrium conditions to provide insight into phase formation. The temperature was set to 1123K to match the experimental conditions because the σ-FeV phase forms when temperature falls in the range of 923–1492K. To predict the equilibrium phase compositions in the Fe–Ti–V and Fe–Cr–V systems as shown in Fig. 13f, thermodynamic calculations were performed to achieve a graded structure from Ti6Al4V to SS 304L [129]. As σ-FeV phase need to be avoided, the calculations of Fe–Cr–V systems in Fig. 13f provide an alternative to changing the composition of 25 vol% SS 304L plus 75 vol% V composition (point B) to 100 vol% SS 304L (point D) directly. However, the σ-FeV phase may still form when layer remelting during fabrication. In essence, these results illustrate how the CALPHAD technique can provide a new pathway to the design FGMs in AM processes.

In other related work, Reichardt et al. [130] also used AM to manufacture a FGM consisting of Ti6Al4V and SS 304L with V as a transition material. Interestingly, cracking occurred at a location corresponding to the same composition as that in the aforementioned study by Bobbio et al. [125]. However, in this study, the authors deposited a sample B that included a reverse transition which started from 100 vol% SS 304L, followed by additions of V in each layer with a 3% increment. Deposition was discontinued at composition corresponding to 64 vol% SS 304L plus 36 vol% V due to crack formation. Moreover, the results of this study demonstrated that interlayer bonding was compromised by the formation of the Fe–V–Cr σ phase. Overall, the results from these studies suggest that V is not suitable as an intermediate material for FGMs consisting of Ti6Al4V and SS 304L [130]. Interestingly, a successful FGM consisting of Ti6Al4V and 304L SS was achieved when a transitional composition (Ti6Al4V→V→Cr→Fe→SS316) was introduced. In this case, intermetallic phases did not form and the highest hardness value was only 425HV, confirming the absence of intermetallic [131].

4.1.3. Ti6Al4V/invar

Bobbio et al. [132] used DED to fabricate FGMs consisting of Ti6Al4V and Invar alloy. In this study, the first 21 deposited layers were pre-alloyed Ti6Al4V powders followed by a transition region with 32 layers. In the transition region, the volume fraction of Ti6Al4V decreased by 3 vol% in each layer with an Invar increment of 3 vol%. Although cracks were observed in the transition region, the fabrication process was successfully carried through to completion with the last 22 layers consisting of 100 vol% Invar. In the transition region, FeTi and Fe_2Ti phases were observed. The residual stresses originating from mismatches in the coefficient of thermal expansion between these two phases were proposed as the reason for the formation of cracks. The sample and its corresponding optical macrograph are shown in Fig. 14a and b. In this work the laser power was operated at 900W with a scanning speed of 12.7 mm/s [132].

Both experimental and computational approaches were used to

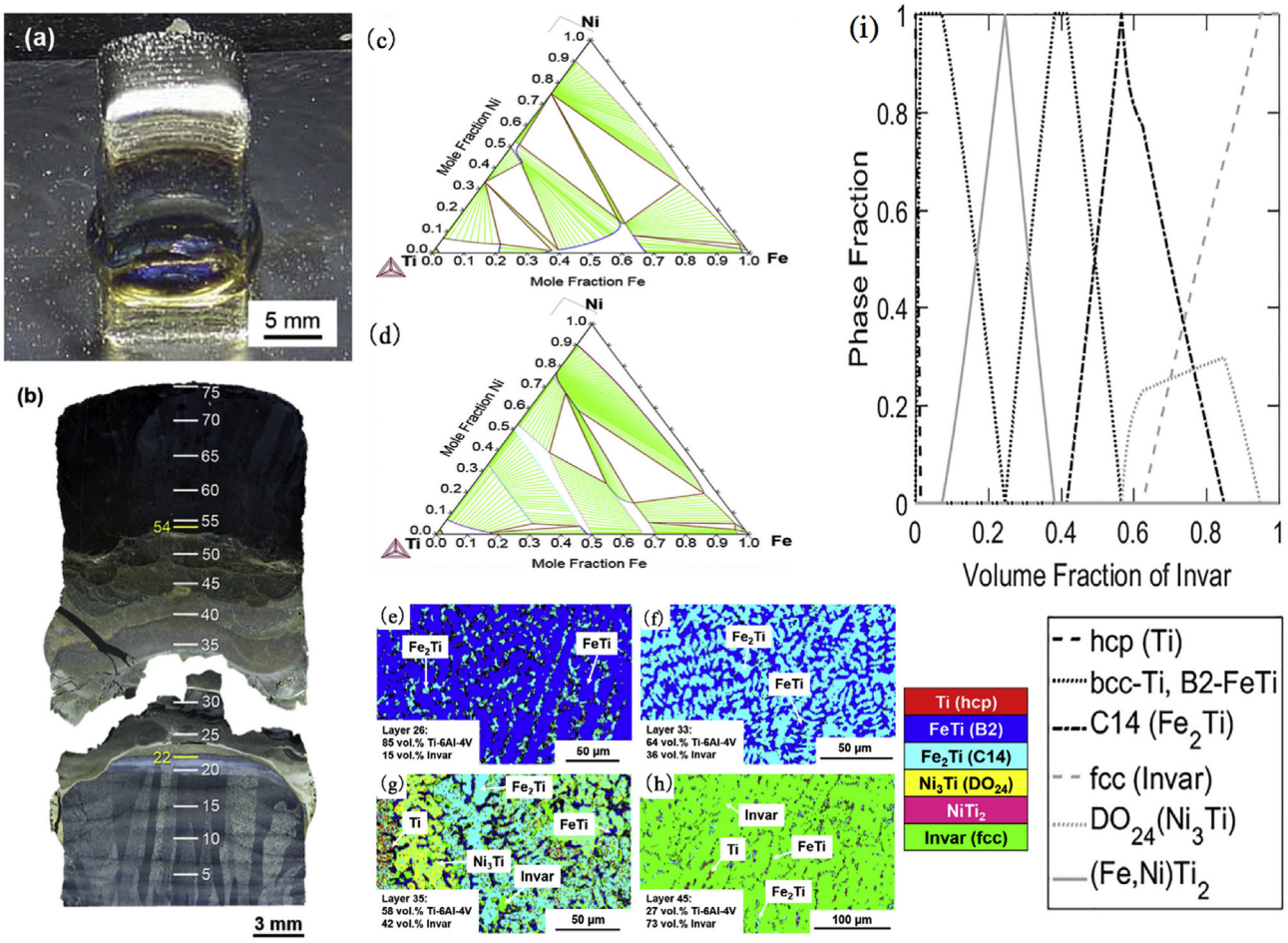

Fig. 14. (a)The FGM sample graded from Ti6Al4V to Invar, (b) optical macrograph of the FGM sample, (c) and (d) phase equilibria computed based on the TCFE8 database and on the assessment [133] of the Fe–Ni–Ti system at 1100K, respectively, and (e) through (h) EBSD phase mapping within the graded region, and (i) atomic fractions of phases as predicted using CALPHAD method [132].

identify the phases in this study. Two different databases are implemented to compute phase equilibria at 1100K, leading to two different phases predicted, as shown in Fig. 14c and d. The computational method used in this study is also CALPHAD, similar to that used in the study of Ti6Al4V to SS 304L with V as transition materials [125]. The results of the computations are presented in Fig. 14i, and show, for example, that the FeTi phase is formed where $NiTi_2$ disappears at composition of 37 vol% Invar. This result is consistent with the experimental findings shown in Fig. 14f; with some differences noted. For a composition of 73 vol% Invar, the presence of a hexagonal close packed (HCP) phase is shown in Fig. 14h which is not consistent with the simulation results. Moreover, a large crack occurred at a composition of 64 vol% Ti6Al4V plus 36 vol% Invar where FeTi and Fe_2Ti formed. The coefficient of thermal expansion of these two phases are significantly different which lead to interlayer fracture [134]. Moreover, a high hardness of 858 ± 18HV was measured for a composition of 36 vol% Invar which likely originates from the presence of the FeTi and Fe_2Ti phases.

4.1.4. Ti6Al4V/Mo

Maunoury et al. [135] used DED to study FG Ti6Al4V/Mo composites. The compositions used in this study are Mo with 25 vol% change in each graded region from 100 vol% Ti6Al4V at the bottom to pure Mo on the top, as shown in Fig. 15a. FG Ti6Al4V/Mo composites were prepared using laser power values of: 1600W, 1800W and 2000W depending on the volume fraction of Mo in the graded region. No cracks or other obvious defects can be observed in the samples.

Fig. 15b shows an EBSD micrograph before and after β -phase reconstruction. Fig. 15c through e show β-phase EBSD micrographs from the bottom to top of the FGM sample. In Fig. 15c through e, the broken lines delineate the interfaces between different graded regions, suggesting a metallurgical bonding between these graded regions, which can be attributed to spanning of β-grains across the interfaces. Hardness measurements were performed from the bottom to top of the FGM sample along three lines apart from 0.75 mm from each other. The hardness increases from 250HV to 450HV with more Mo introduced from the bottom to top, but drops to the lowest value of 190HV in the region of pure Mo [135], as shown in Fig. 15f.

4.1.5. Ti6Al4V/Al_2O_3

FGMs Ti–Al are of interest when performance requirements include high strength and low density [136,137]. In related work, Zhang et al. [138] prepared a FG Ti6Al4V/Al_2O_3 composite via LENS. The starting powders were sieved in the range of 44–74 μm and laser power density was precisely controlled from 385W to 420W to achieve good building performance. As a result of the high laser absorption ability of Al_2O_3, the gradient region containing Al_2O_3 must be fabricated using a laser power higher than 400W. Fig. 16a presents the photograph of the FG Ti6Al4V/Al_2O_3 composite manufactured, together with the composition and height of each region. Fig. 16b shows microstructure in the region containing Ti6Al4V substrate and LENS fabricated Ti6Al4V, and a smooth transition between the two materials is evident. Fig. 16c demonstrates microstructure in the region including LENS fabricated Ti6Al4V and Ti6Al4V plus Al_2O_3, and a sharp interface exists between

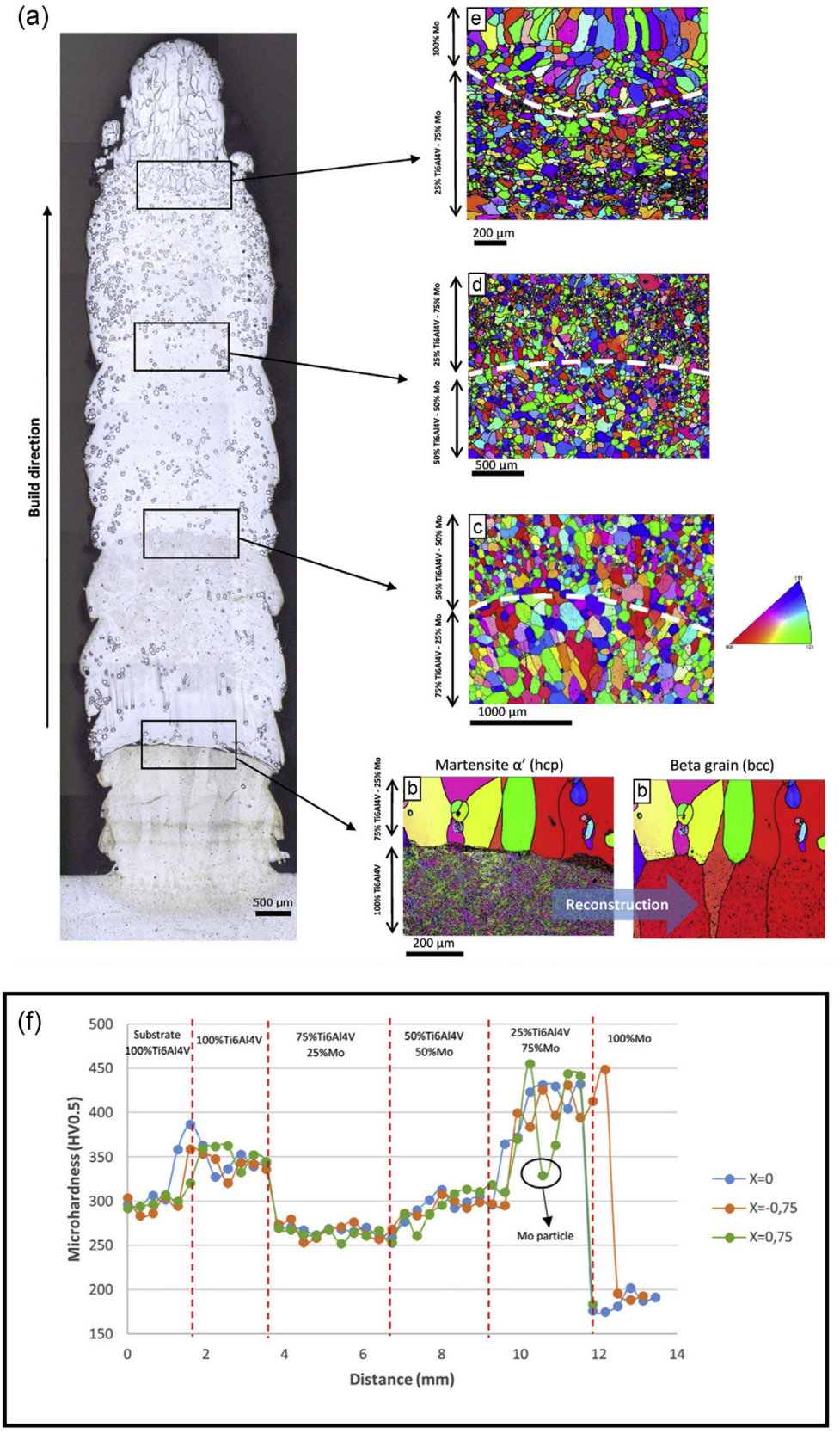

Fig. 15. (a) photograph of FG Ti6Al4V/Mo composite, (b) EBSD micrograph before and after β -phase reconstruction at the interface between 100 vol% Ti6Al4V and 75 vol% Ti6Al4V plus 25% Mo corresponding to the rectangular region in (a), (c) through (e) EBSD micrographs of β-phase, corresponding to the rectangular regions in (a), respectively, where broken lines delineate interfaces between graded regions with different compositions, and (f) microhardness of FG Ti6Al4V/Mo from the bottom to top along three lines apart from 0.75 mm [135].

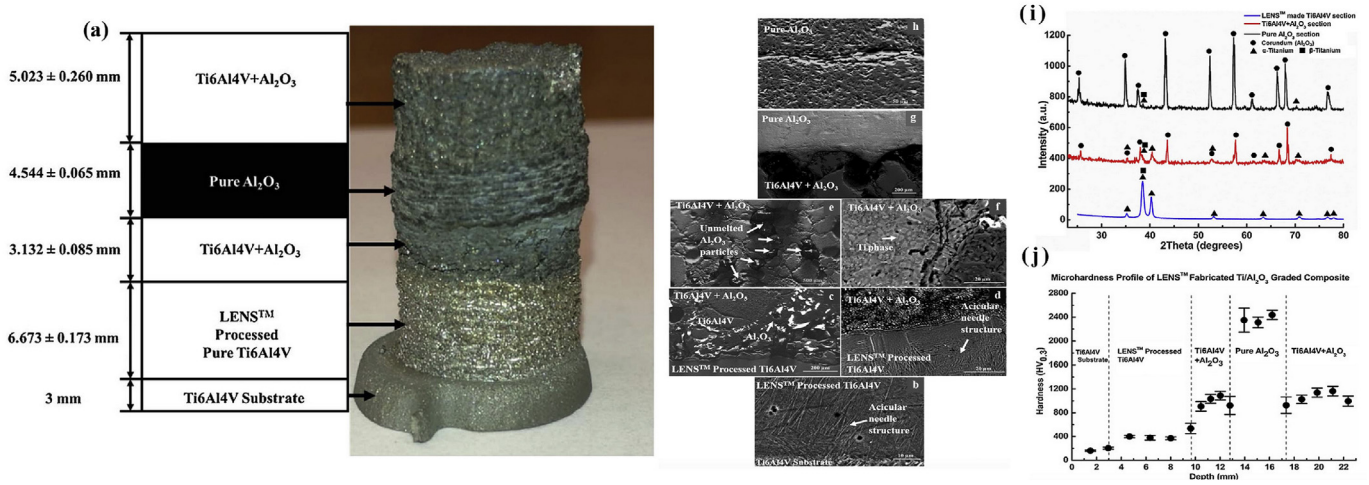

Fig. 16. (a) photograph of the FG Ti6Al4V/Al_2O_3 manufactured, together with the composition and height of each region; (b) SEM micrograph showing microstructure in the region containing Ti6Al4V substrate and LENS fabricated Ti6Al4V; (c) SEM micrograph showing microstructure in the region including LENS fabricated Ti6Al4V and Ti6Al4V plus Al_2O_3; (d) higher magnification micrograph of (c); (e) SEM micrograph showing microstructure in the region comprising Ti6Al4V plus Al_2O_3 only; (f) higher magnification micrograph of (e); (g) SEM micrograph showing microstructure in the region consisting of Ti6Al4V plus Al_2O_3 and Al_2O_3; (h) SEM micrograph showing microstructure in the region with Al_2O_3 only; (i) XRD results; (j) Microhardness from the bottom to top of the FG Ti6Al4V/Al_2O_3 [138].

Ti6Al4V and Ti6Al4V plus Al_2O_3. To better highlight this region, a higher magnification micrograph of Fig. 16c is also provided, as shown in Fig. 16d. Fig. 16e shows the microstructure in the region comprising Ti6Al4V plus Al_2O_3 and only unmelted Al_2O_3 particles are present in the region as a result of an increase in scanning speed. Again, a higher magnification micrograph of Fig. 16e is shown in Fig. 16f. On the one hand, a higher scanning speed leads to inadequate melting and hence the formation of unmelted Al_2O_3 particles. On the other hand, a higher scanning speed reduces the residual thermal energy and eliminates defects, e.g., porosity, cracks, poor bonding between powders, during fabrication. In other words, scanning speed and laser power density clearly present a trade-off in this study. Inspection of Fig. 16g reveals the absence of delamination between the region of Ti6Al4V plus Al_2O_3 and the region of Al_2O_3, although there are micro-cracks and porosity at the in the interface between the two regions, likely attributable to the internal stress generated during laser heating [139]. Fig. 16h shows the microstructure in the region that contain only Al_2O_3. Based on XRD results in Fig. 16i, α-Ti and β-Ti phases are identified in the region containing only Ti6Al4V; corundum and Ti phases are detected in the region consisting of Ti6Al4V + Al_2O_3; and the corundum phase is present in the pure Al_2O_3 region as well. The hardness results as shown in Fig. 16j are consistent with the XRD analysis, with the highest hardness value of 2365.5 ± 64.7 HV corresponding to the region comprising of only Al_2O_3 and a hardness value of 1000HV in the region consisting of Ti6Al4V + Al_2O_3.

A similar study was performed by Yin et al. [140] using a combined approach to fabricate FG Ti6Al4V/Al_2O_3. In this study, a substrate of Ti6Al4V was fabricated using a laser melting technique, and the graded regions were fabricated using a cold spray technique. Unfortunately, the presence of multiple cracks and pores effectively degraded the mechanical behavior of the deposited material.

For purpose of comparison, the reported mechanical properties of Ti-based FGMs processed by AM are summarized in Table 3.

4.2. Fe-based alloys

Iron and its alloys, namely steel, are widely used as a structural material in a broad range of engineering applications because of their low cost, high strength and longevity as a structural material. By altering carbon and other elemental contents within steels, their precise mechanical performance can be engineered for specific applications, such as corrosion resistance, for example [141]. Steels are also frequently used as the structural backbone for other more expensive materials, but the dissimilar microstructures and physical properties often make these joins difficult. The integration of FGMs processed by AM has been demonstrated as a promising method of fabricating these types of materials [142,143].

4.2.1. SS 316L

Various investigators have studied the influence of AM parameters on the evolution of localized heterogeneities in an effort to optimize functional designs for specific applications. As such, studies have been conducted in an effort to additively manufacture different grain morphologies for systems such as AlSi10Mg [144], IN718 [145] and Ta [146]. In the case of SS 316L, for example, Amine et al. [147] systematically investigated multilayered SS 316L, and found that an increased cooling rate during solidification can produce fine grains with a corresponding high hardness. Moreover, the hardness also increased with increasing scanning speed and lower laser power.

Niendorf et al. [148,149] used SLM to manufacture FG SS 316L containing regions with different local functionalities, as schematically shown in Fig. 17a (see grey regions), which were fabricated using laser powers ranging from 400 to 1000 W. The two grey regions (one marked by a red circle) exhibit higher strain magnitudes relative to other regions when the FG SS 316L was subjected to an applied stress, as shown in Fig. 17a. In addition, after heat treatment at 650 °C for 2 hours, the average microhardness was measured to be 150 and 220HV in grey regions and in other regions, respectively, as presented in Fig. 17b. Moreover, the tensile properties in the grey and other regions are reported in Fig. 17c. The other regions exhibit a yield strength higher than that in the grey regions, which even approaches the ultimate tensile strength in grey regions. EBSD analysis indicates that the regions are characterized by columnar coarse grains and equiaxed fine grains, respectively, as illustrated by the EBSD inverse pole figure in Fig. 17d. The inverse pole figures in Fig. 17e and f shows strong < 001 > fiber intensities in the columnar coarse grained regions but weak intensities along < 001 > , < 101 > and < 111 > in the equiaxed fine grained regions, respectively.

4.2.2. SS 316L/Stellite 12

Stellite alloys and their composites are of interest for wear and corrosion resistant applications [150,151]. Laser cladding and cold

Table 3
Reported mechanical properties of Ti-based FGMs processed by AM.

Material	AM Technology	Elastic Modulus (GPa)	Yield Strength (MPa)	Ultimate Tensile Strength (MPa)	Elongation (%)	Hardness (HV)
Ti6Al4V/TiC [89] From 0% to 50%TiC	LMD	n/a	n/a	750–1200	0–5.5	380–737
TA15/TiC [93] From 0% to 50%TiC	LMD	n/a	806–925	886–1085	1.23–4.32	n/a
Ti6Al4V/TiC [101] From 0% to 30%TiC	DED	108–164	n/a	551–991	n/a	300–600
Ti6Al4V/SS304 L/V [125]	DED	n/a	n/a	n/a	n/a	220–850
From pure Ti6Al4V to50%V/50%SS304L	DED	n/a	n/a	n/a	n/a	190–900
Ti6Al4V/Invar [132] From pure Ti6Al4V to pure Invar with 3% increment.	DED	n/a	n/a	n/a	n/a	350–858
Ti6Al4V/Mo [135] From pure Ti6Al4V to pure Mo with 25% increment.	DED	n/a	n/a	n/a	n/a	250–450
Ti6Al4V/Al_2O_3 [138]	LENS	n/a	n/a	n/a	n/a	350–2365

(LMD: Laser Melting Deposition, DED: Directed Energy Deposition, LENS: Laser Engineered Net shape).

spraying techniques have been used to coat Stellite onto steels for enhanced performance [152,153]. Alternatively, Yakovlev et al. [154] experimented with various FG SS 316L/Stellite 12 composites produced by a coaxial powder injection approach. Although the two alloys share similar bulk properties, the larger Stellite particle size require a higher laser power (120W) relative to that used for steel (90W). By changing the laser power according to the designed composition (premixed SS 316L and Stellite 12 powder), a smooth transition from steel to Stellite with a gradient zone as small as 1 μm can be produced as shown in Fig. 18a. Stellite has dendritic microstructure that consisting of a Co–Cr–W solid solution, mono-carbides ($M_{23}C_6$ and M_7C_3) and intermetallic compounds such as Co_3W. As evident from Fig. 18b, these soft matrices are gradually replaced by the addition of SS 316L, which leads to changes in mechanical properties. In Fig. 18c, the microhardness for such sample increased gradually from around 200HV to above 600HV. In Fig. 18d, the SEM image of FG SS 316L/Stellite with direct joining between SS 316L and Stellite is observed to have a sharp gradient. The sample possesses a smooth oscillating microhardness value around 300HV and 400HV due to the relatively small transition zone of 70 μm (shown in Fig. f) [154].

4.2.3. SS 316L/Cu

In an effort to fabricate FGMs with compositional variations along the vertical direction, Liu et al. [155] installed a center separator on a

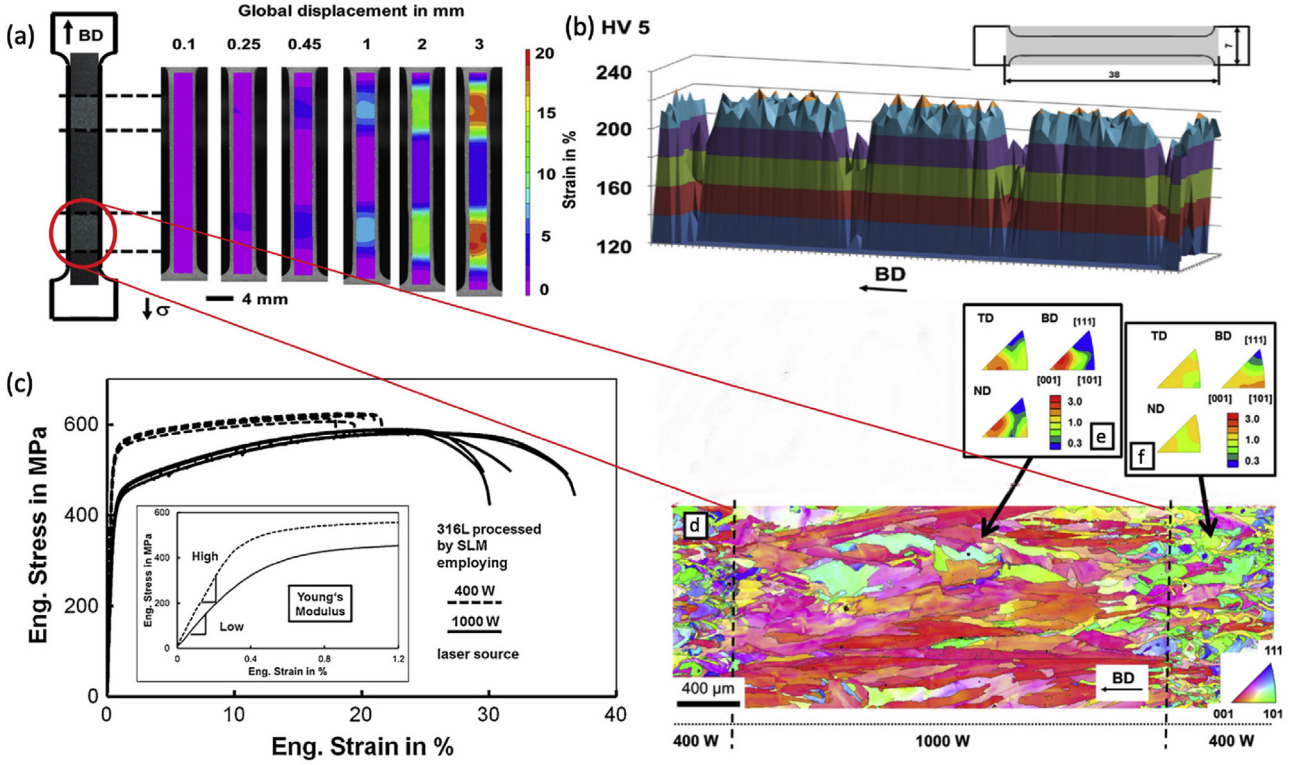

Fig. 17. (a) FG SS 316L containing the regions with different local functionalities, together with the strains in different regions, (b) microhardness distribution in the FG SS 316L, (c) tensile engineering stress vs. strain curves in the regions fabricated using laser power 400 and 1000 W, respectively, (d) EBSD inverse pole figure showing equiaxed fine grains (other regions) and columnar coarse grains (grey regions) fabricated using laser power 400 and 1000 W, respectively, e) strong < 001 > fiber intensities in columnar coarse grained regions, and f) weak intensities along < 001 > , < 101 > and < 111 > in equiaxed fine grained regions [148,149].

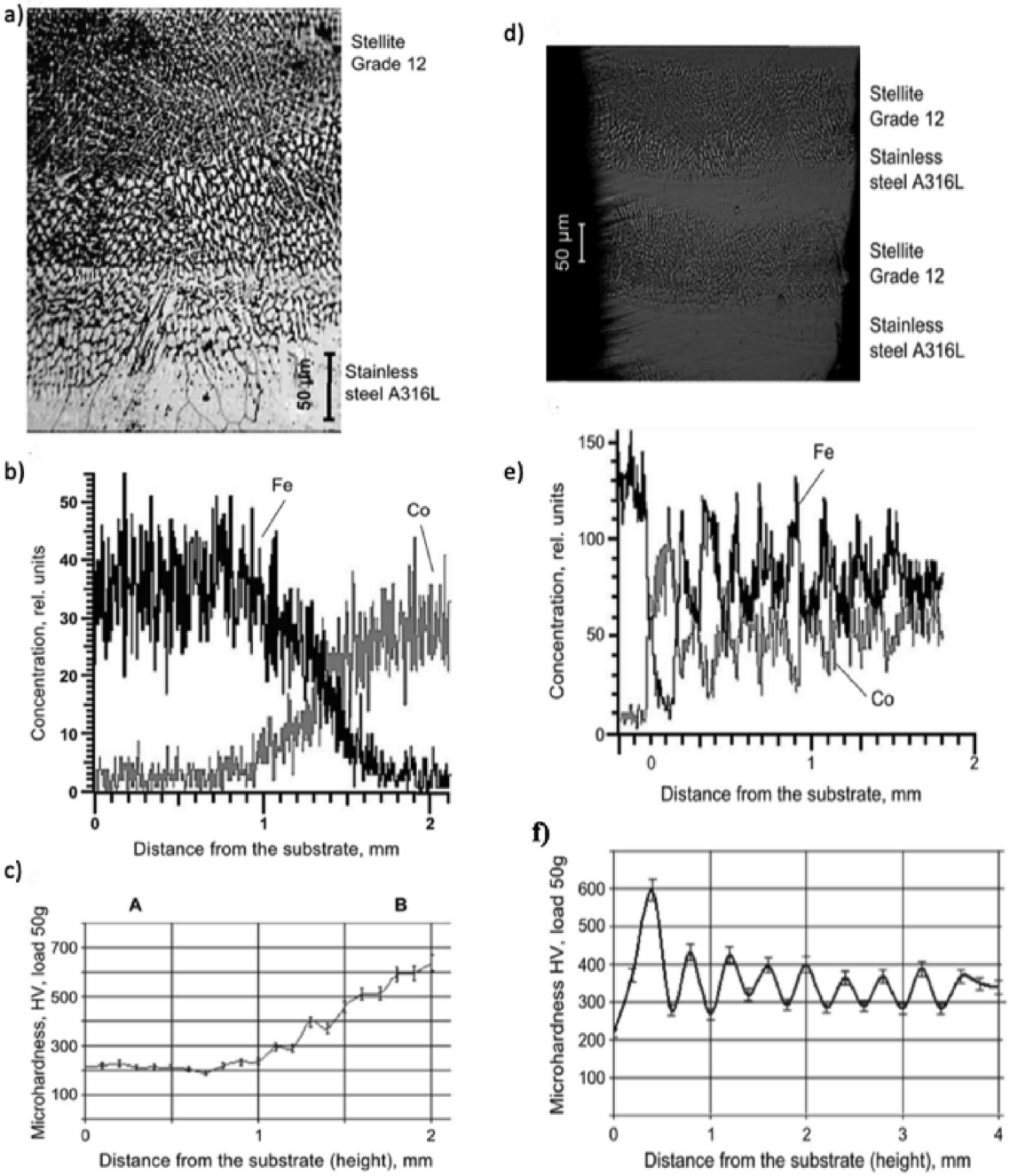

Fig. 18. (a) SEM image of FG SS 316L/Stellite 12 composite with (b) elemental analysis and (c) microhardness transition. (d) SEM image of FG SS 316L/Stellite composite with alternating layer with (e) elemental analysis and (f) oscillation of microhardness values [154].

laser system so that each nozzle dispensed only the corresponding powder. Using this modified system, they successfully fabricated bi-metallic steel/Cu laminar. Although the SS 316L section exhibited only a few pores, the Cu section revealed a high-volume fraction of pores, likely attributable to incomplete melting because of Cu's high reflectivity and thermal conductivity. As a result, the tensile test fractures are initiated mostly on the copper side (Fig. 19a), which suggests that bond strength of the steel/Cu region is higher that corresponding to the Cu region (e.g., 49 ± 10.3MPa). Because of the fast cooling rate associated with SLM, fine grain sizes around 1–10 μm were reported. The ultimate tensile strength for the FG specimen falls in between that of the two individual components, where ultimate tensile strength of SS 316L ranges from 310±18Mpa to 726± 2.6Mpa and 49± 10.3Mpa of Cu, respectively. The hardness values display a smooth variation from 259HV to 74HV relative to the stainless steel and copper regions (Fig. 19b).

4.2.4. SS 316L/P21Ferritic steel

Woo et al. [82] used DED to manufacture a FG SS 316L/P21 ferritic steel composite with different compositions using different build path strategies. The DED process was performed using a laser power ranging from 200 to 1000 W. An automatic feedback control system that adjusts the laser power (INSSTECK MX-400) was used to maintain the layer thickness (250 μm) and hatch width (400 μm) during the deposition process. Five building strategies were tested, which are described as follows: horizontal with uniaxial scan that produces 100 vol% SS 316L to 100 vol% P21 bimetallic composition in case 1; uniaxial scan that changes SS 316L composition from 100 vol% to 50 vol% to 0 vol% in case 2; uniaxial scan with SS 316L composition varying from 100 vol%

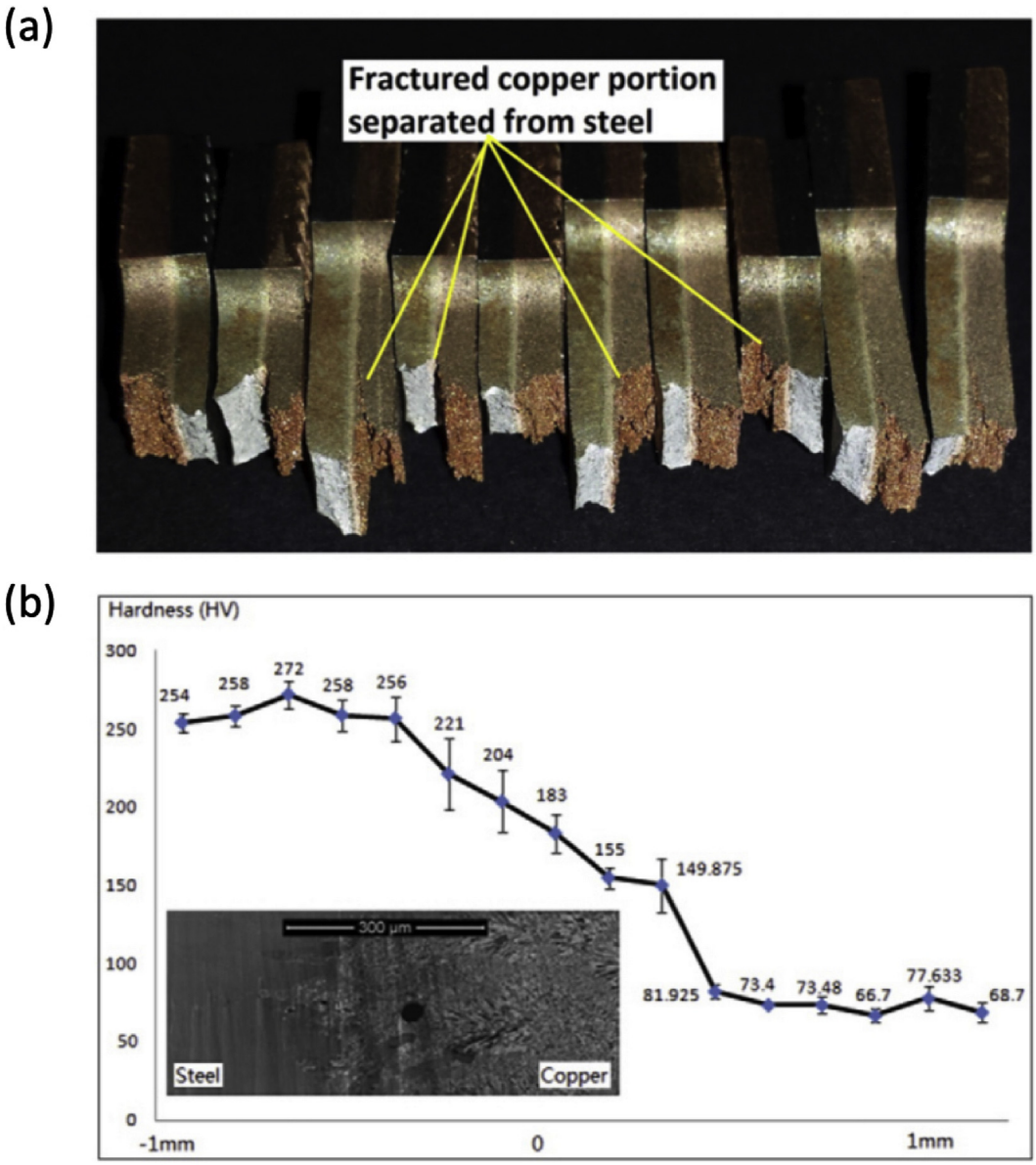

Fig. 19. (a) fracture surface of 316L SS/Cu samples (b) hardness value transition from steel to Cu [155].

to 0 vol% with 25 vol% decrement in case 3; orthogonal scan in case 4 using the same composition as that used in case 3; and an island scan strategy in case 5 using the same composition as that used in case 3. From case 1, as illustrated in Fig. 20a, both SS 316L and P21 show an equiaxed grain structure created by the epitaxial grain growth along the build direction. In Fig. 20b corresponding to case 2, the SS 316L section grows into much larger grains, while for case 3 (Fig. 20c), the P21 regions have also experienced grain growth (e.g., coarser grains). In Fig. 20d–e, cases 4 and 5 exhibit finer grains and smoother transitions. Preferentially inclined grain structures in the P21 sample form from uniaxial scans, while it is less so for the orthogonal scan and the island scan exhibits smaller grains. These localized microstructural changes effectively reduced the residual stress from the 680 MPa of orthogonal scan to the 430 MPa of island scan. The hardness increases from 200HV to 440HV as the grain size decreases from the 316L regions to the P21 [82]. An investigation of the same system was reported by Kim et al. [156], for which the FG 316L/P21 composite shows much reduced elongation from 33.9% for 316L to 10.3% to P21 but with much higher yield strength ranging from 530 MPa to 970 MPa and ultimate tensile strength ranging from 660 MPa to 1360 MPa. In their investigation of the microstructure, the cause for mechanical performance improvement was argued to be related to the austenite phase distributed in α' martensite.

4.2.5. SS 316L/NiCr

Zhang et al. [157] used a YLS-6000 laser melting system to manufacture an FG 316L SS with Cr/Ni alloy. Five wt.% ratios of Cr/Ni alloy corresponding to 1.4, 1.7, 2.3, 3.7 and 9.7 were printed on a 316L SS substrate. No obvious defects were found on the SS 316L substrate, and columnar dendrites grew epitaxial throughout different layers of Cr/Ni. The phase transition occurs in such order that γ-Fe to γ-Fe + α-Fe, then from γ-Fe + α-Fe + $(Cr, Fe)_7C_3$ to α-Fe + $(Cr, Fe)_7C_3$ as the Cr/Ni ratio increases. The authors reported a smooth microstructure as well as a smooth transition of microhardness which they argued were indicative of strong bonding in the sample. The maximum hardness attained was 6.90 GPa corresponding to a Cr/Ni ratio of 9.7.

4.2.6. SS 316L/IN718

Hinojos et al. [158] studied the joining of IN718 and SS 316L using an Energy Beam Melting (EBM) S12 system. In this study, both

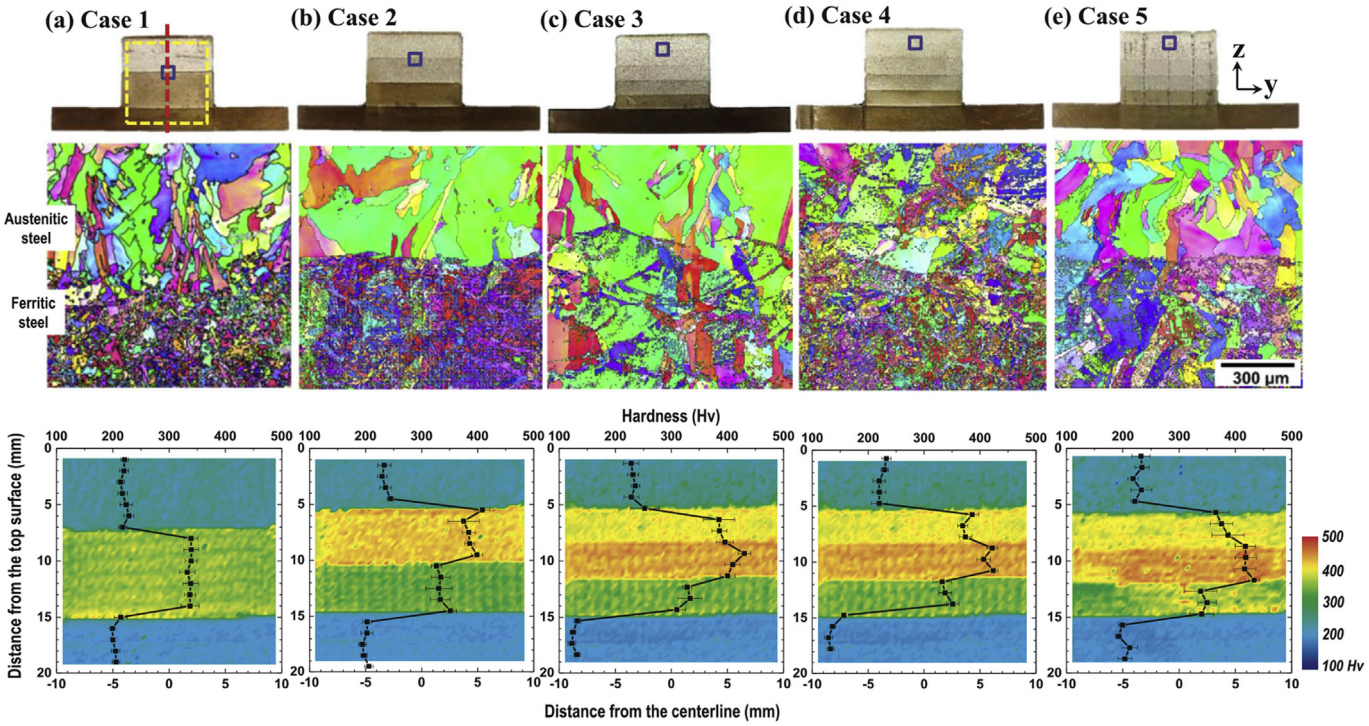

Fig. 20. Cross-sections, morphologies and hardness of five FG SS 316L/P21 [82].

materials were used as substrate materials to avoid using other filler materials. The filler materials used in-between the two main alloys change the overall chemical composition of the FGMs to act as a buffer to their dissimilarity in physical properties and a filler for defects within the interface region. To avoid compromising the integrity of the initial chemical composition, the use of filler materials needs to be avoided. Directly depositing one main material onto the other leads to the formation of a small heat affected zone depth (443±56 μm) which minimizes the change in hardness of IN718 and 316L SS near their interface, which are approximately 296 and 148 HV, respectively. In related work, Shah et al. [159] studied the behavior of FG SS 316L/IN718 composites containing 25 vol%, 50 vol% and 75 vol% compositions of IN718 as an intermediate layer in the transition area. Their results show that columnar dendrites appear throughout different compositions, as can be seen in high magnification images (Fig. 21a). Around the interfaces of the two graded layers, the dendrites change into a cellular morphology, which is particularly evident in the case of 75 vol% SS 316L shown in Fig. 21a. The predominantly columnar microstructure provides good bonding between layers, and the change of dendrites from columnar to cellular does not appear to be detrimental to the integrity of the entire sample, as no drastic fluctuations in hardness values as a function of position are evident. Interestingly, in Fig. 21c–d, the hardness value plots reveal a parabolic shape instead of a constant decline. The increase of hardness has to do with the NbC formation when content of IN718 reaches 50 vol%, which was observed through XRD in Fig. 21b. In this case, the secondary phase, NbC, enhances the strength of the sample without embrittling it to the point of fracture. The effects of the laser power and powder flow rate on the hardness were also studied as shown in Fig. 21c and d. The results show that the hardness decreases with increasing laser power and powder flow rate, which is consistent with results from another study on IN718 [160]. To increase the heat input by increasing the laser power and powder flow rate will accelerate grain growth in the sample, as a result reducing the mechanical strength.

4.2.7. SS 410/NiCr/Ti6Al4V

Sahassrabudhe et al. [117] studied a FG SS 410/Ti6Al4V composite with and without an NiCr layer by using LENS. The fabrication of the FG SS 410/Ti6Al4V composite was unsuccessful due to the formation of brittle intermetallic phases (e.g., FeTi) and related residual stresses that ultimately caused delamination. As a result, their results show that hardness rapidly increases from approximately 115 HV in SS410 to 275 HV in Ti6Al4V. To minimize thermal and residual stresses for these bimetallic structures, an NiCr layer was deposited between the SS 410 and Ti6Al4V. With this configuration, the sample shows a smooth transition from SS 410 to the NiCr layer. Moreover, a graded transition layer was observed in the region from NiCr to Ti6Al4V with the newfound presence of “globules” throughout the Ti6Al4V layer. These “globules” are around tens of microns in diameter, but the chemistry and the microstructural significance of which had not been investigated further. The authors also documented the presence of Cr_2Ti and NiTi intermetallics, although these phases did note appeared to play a role in early crack formation. The hardness of the NiCr and NiCr/Ti6Al4V regions are approximately 130 HV and 120 HV, respectively.

4.2.8. SS 316L/Fe_3Al

The superior crack resistance, under stress corrosion conditions, of Fe_3Al [161,162], has led to interest in FG SS 316/Fe_3Al composites because the susceptibility of 316L SS to fracture under pressure and heat can be prevented by a Fe_3Al layer [163]. Durejko et al. [164] fabricated thin wall tubes of Fe_3Al/SS 316L using LENS. By first modifying the PartPrep programme for FGMs with radially varying composition, tubular samples of a few millimeters wall thickness were generated and built. Despite the presence of some surface cracks, no cracks are found to propagate in the body of the samples. Elongated grains are observed across interfaces of each graded layers, as a result from the smooth transition between SS 316L and Fe_3Al. The values of microhardness are approximately 500HV at SS 316L and 400HV at Fe_3Al.

4.2.9. SS 304L/IN625

Carrol et al. [40] fabricated a FG SS 304L/IN625 with 24 layers of graded transition zones using DED. The microstructure of the product changes from the typical austenitic to cellular dendrites when the

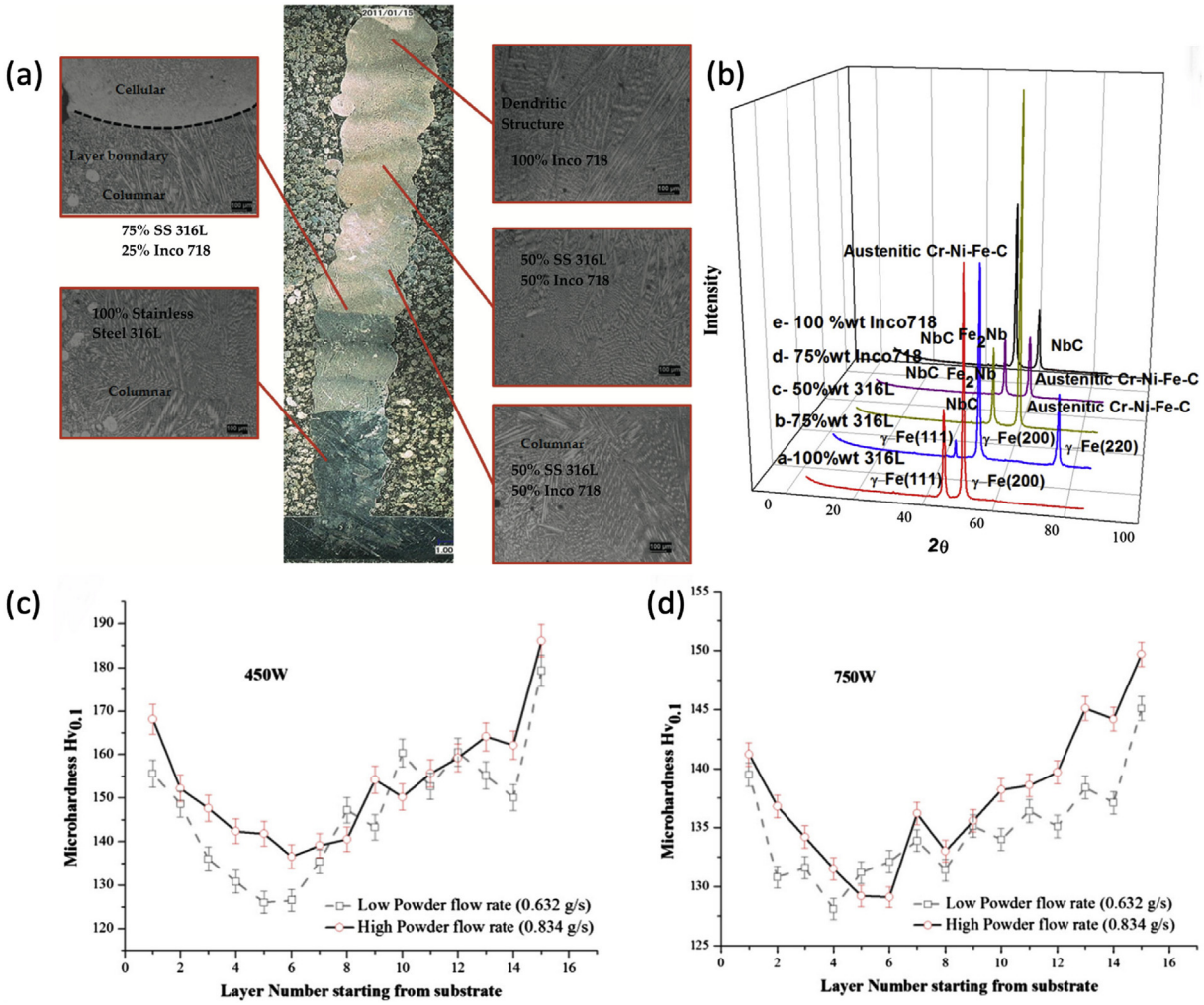

Fig. 21. (a) Overall structure and SEM of microstructures of different graded SS 316L/IN718 layers showing presence of columnar and cellular dendrites, (b) XRD patterns showing NbC phase formation at 50 vol% IN718, (c–d) parabolic hardness values for 450W and 750W laser power at different powder flow rate [159].

composition changes from 15 vol% to 50 vol% of IN625. Then, the columnar dendrites are formed at the region with 50 vol% IN625. Cracks are observed at the region with 79 vol% SS 304L. To provide insight into the mechanism responsible for crack nucleation, they studied the distribution of elements using EDS, as shown in Fig. 22 a-h. The results show that high concentrations of Mo, Nb and C are present near the crack, and little of the said elements is observed farther away from the crack. This result suggests the formation of compounds among Mo, Nb and C that lead to the formation of the final macroscopic crack. In addition, the thermodynamic simulations predict that the stable Mo and Nb monocarbides will form under the processing conditions used, as shown as the phase diagrams in Fig. 22 i-j. The hardness values of the sample were reported to be 196HV for IN625 to 250HV for SS 304L.

4.2.10. Fe/Cr/Ni

Fe–Cr–Ni based alloys can be engineered to yield different phase compositions, and as such have attracted attention as candidate FG materials. In related work, Li et al. [165] produced FG Fe/Cr/Ni with four different compositions based on the Fe–Cr–Ni ternary phase diagram in Fig. 23a and calculated the associated mixing enthalpy for: Fe–9Cr–28Ni, Fe–12Cr–23Ni, Fe–14Cr–16Ni and Fe–16Cr–8Ni, as shown in Fig. 23b. The four compositions enable phase transformations between austenite and ferrite, moreover, with increasing Ni content, the mixing enthalpy becomes more negative, which favors a phase transformation from ferrite to austenite. A more tightly spaced ferritic and austenitic lath morphology were found in Ni-scarce regions, while a segregated austenite solidification structure was observed in N-rich regions as shown in Fig. 23c–d. These two types of microstructures result in different mechanical properties. The decrease in hardness indicates the transition from the harder ferritic phase to the softer austenite phase. In Fig. 23e, the inclusion of the soft and ductile austenite phase into the more compact microstructure reduces the strength as the values of hardness decreases gradually from 250HV at Cr-rich region to 110HV at Ni-rich region.

4.2.11. Other steel FGMs

In addition to the systems discussed, SS 316L, AlBrnz, Colmonoy 6, Stellite 6, 420 SS and H13 tool steel have all been manufactured through directed metal deposition (DMD) in individual components, FGMs, and wafer composites on POM 505 systems [166]. During the manufacturing process, both the substrate and the deposited powder were melted and solidified rapidly to minimize the size of the heat affected zone. The coefficient of thermal expansion for FGMs tend to be lower than that for the individual alloys. In addition, a dilution effect has been found between AlBrnz and 420 SS due to the subsequent deposition onto the prior high temperature deposited material. AlBrnz was also found in the form of dendrite precipitates in the SS 420 phase [166]. For FG SS 316L/H13 tool steel composite (shown in Fig. 24a) and FG SS 316L/Colmonoy composite (shown in Fig. 24b), the strength and plasticity of the composites represent the average values of the individual components. It can be seen from Fig. 24c that the FG SS 316L/SS 420 composite exhibits higher yield strength and ultimate

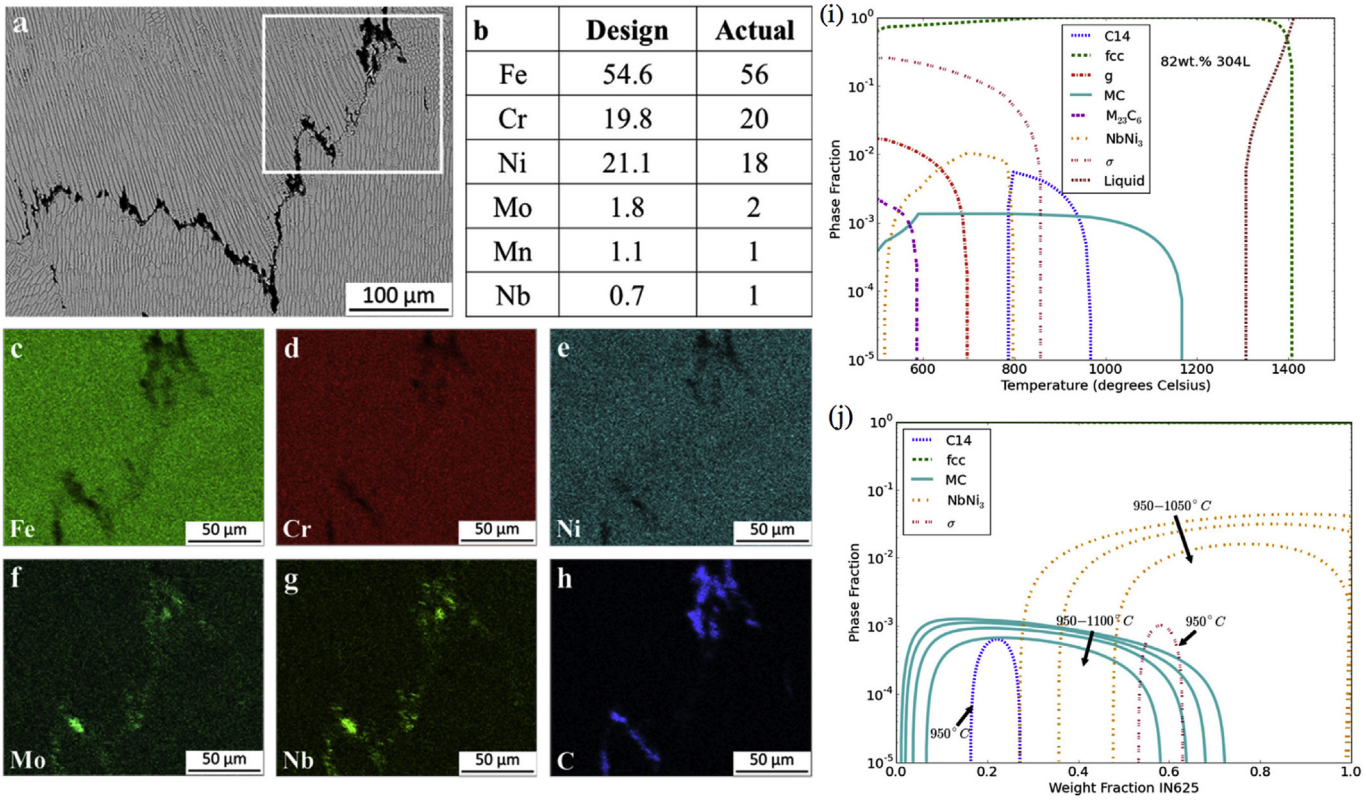

Fig. 22. (a) BSE imaging on the crack at 79 vol% SS 304L, (b) comparison of designed element composition and measured composition, (c–h) EDS images for different elements, (i–j) phase diagram showing stable monocarbide phases at working temperature [40].

tensile strength than that corresponding to the two individual alloys. Although the FG SS 420/AlBrnz composite has lower elongation and ultimate tensile strength compared to the two individual alloys, it displays a significantly higher yield strength in Fig. 24d [167].

The tested hardness values for Fe-based cases are summarized in Table 4.

4.3. Functionally graded porous scaffolds

Metal alloys with porosity gradients are actively being considered for applications such as orthopedic implants. However, these alloys possess a much higher elastic modulus (110–210 GPa) than human bones (3–20 GPa), which can result in material failure due to a stress shielding effect [168]. Many studies have focused on reducing the stiffness of titanium alloys to reduce stress shielding effect, and different models were proposed by researchers to predict the mechanical performance of porous alloys with lattice structural designs [169]. By integrating FGMs concept into the designs of a lattice scaffold, the heterogeneous structures enable the implant component to perform better in human bodies. As the human bone consists of a marrow core, a cortical outer layer, and porous areas in between, FGMs with graded porosity could mimic such hierarchical structure to improve the osseointegration (fixation of synthetic material on bones) of the implant [170]. Conventional manufacturing techniques could also be used to produce porous FGMs; one such study involved sequential compaction, space-holder removal and sintering [171]. However, AM in structural designs give rise to significant opportunities for control and optimization given the wide range of complex geometries that AM technologies can easily produce [48].

4.3.1. Titanium scaffolds

Fousová et al. [43] manufactured graded, porous Ti–6Al–4V alloy and thoroughly studied the microstructure, mechanical properties and the in vitro response (experiment of a body's response to external implant under laboratory conditions). In this study, the samples were produced using SLM with a 200W fiber YB-YAG laser. The printed samples underwent 820 °C heat treatment in an argon environment for 1.5 h and furnace-cooled to 500 °C. This process produces Ti6Al4V with fine grains and a laminar microstructure, but internal porosity and unmelted particles at the surface were noted. The fine microstructure contributed to high tensile and compressive strength; however, the manufacturing defects such as internal pores and unmelted particles reduced the strength, and rendered the sample more susceptible to crack formation. Onal et al. [172] produced three uniform (0.4, 0.6, 0.8 mm strut diameter) and two graded (dense-in, dense-out) Ti6Al4V scaffolds with BCC structure via SLM. The compressive strength values of these scaffolds were directly linked to the overall density as shown in Fig. 25, which places the FGMs in the middle of the pack. In the pre-osteoblast cells seeding experiment, both 0.4 mm uniform and dense-in FGMs samples possess enough space within the scaffolds for successful cell proliferation. Yet, the denser core of the dense-in FG sample has twice the compressive stress tolerance in comparison with the uniform sample. Apart from preferable strength, graded samples demonstrate a less abrupt deformation process unlike uniform samples [42]. The deformation process begins from the thinnest strut layers to the thickest in a layer by layer fashion, as it is also the case for other shaped lattices like cubic and honeycomb [172].

While porosity has been a major factor influencing osseointegration of bone implants, the work of Li et al. [173] reported that even for the same amount of porosity, different implant designs could experience different bone ingrowth progress. The surface area of struts connecting individual pores was pointed out to be another parameter to design for. The minimal surface structures, which possess comparatively greater surface area for any given porosity, provide exceptional mechanical efficiency and sufficient open space for bone ingrowth. For example, Hsieh et al. [174] showed that spinodal shell structures with minimal

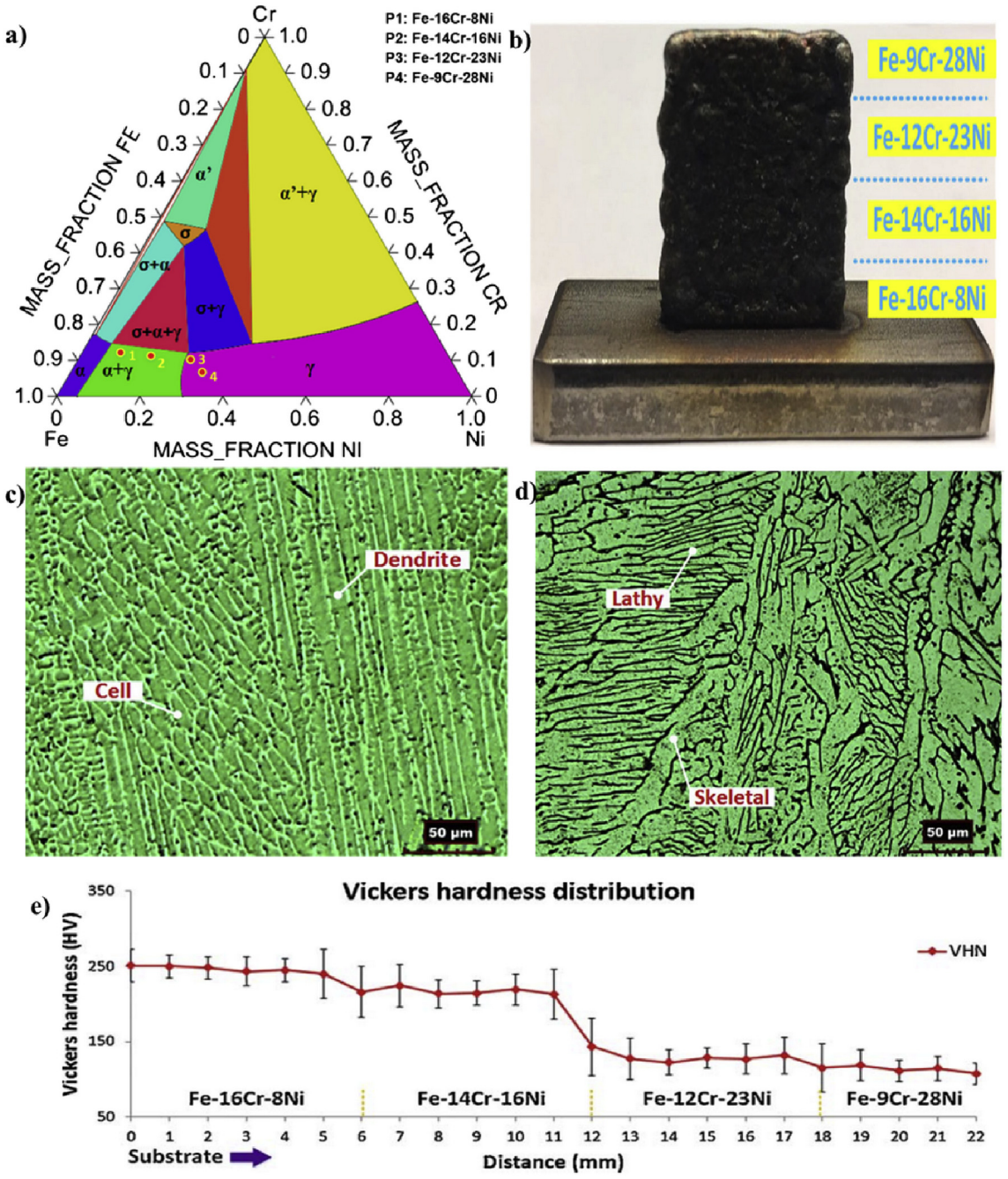

Fig. 23. (a) Ternary phase diagram used for composition selection (b) 3D metallic thin wall sample, (c) microstructure at Ni-rich region, (d) microstructure at Cr-rich region, and (e) hardness change from substrate up [165].

surface characteristics have supreme strength (approaching the theoretical isotropic bound) at high porosity (90%–99%). Other examples are the triply periodic minimal surface (TPMS) structures such as gyroid and diamond structures. Liu et al. [175] used a SLM with 200W CW ytterbium fiber laser to produce graded cellular structures with gyroid and diamond cells. Heat treatment and ultrasonic cleaning were performed before testing and the results showed that the diamond structure exhibits a more uniform stress distribution, while the gyroid structure gives better ductility and ultimate strength [176].

For these complex lattice and cellular structures, finite element analysis (FEA) provides important design information by calculating the deformation behavior of the structures for a given loading condition under different environments. In related work, Xiao et al. [176] used FEA to predict the dynamic and static loadings of FG Ti6Al4V lattice structures. The calculation accurately predicted the initial collapse behavior and indicated that design gradients and loading direction were not consequential to dynamic the response of graded lattice. Zhang et al. [177] manufactured a cylindrical Ti6Al4V specimen with radially graded layers having porosity varying from 91.3 vol%, 76.9 vol %, 48.4 vol% to 21.0 vol%. They also complemented the study by comparing experimental compressive test measurements with three finite element predictions (quarter-symmetric, ideal RVE and defect-coupled RVE). As shown in Fig. 26a and b, the manufactured specimen possesses low density, moderate elastic modulus and high strength values, which differ by only 2% from the simulated mechanical properties. Apart from simulation of mechanical loading behavior, other types of simulation can also be performed to recreate biomedical treatments. For instance, Olivares et al. [178] modelled the perfusion

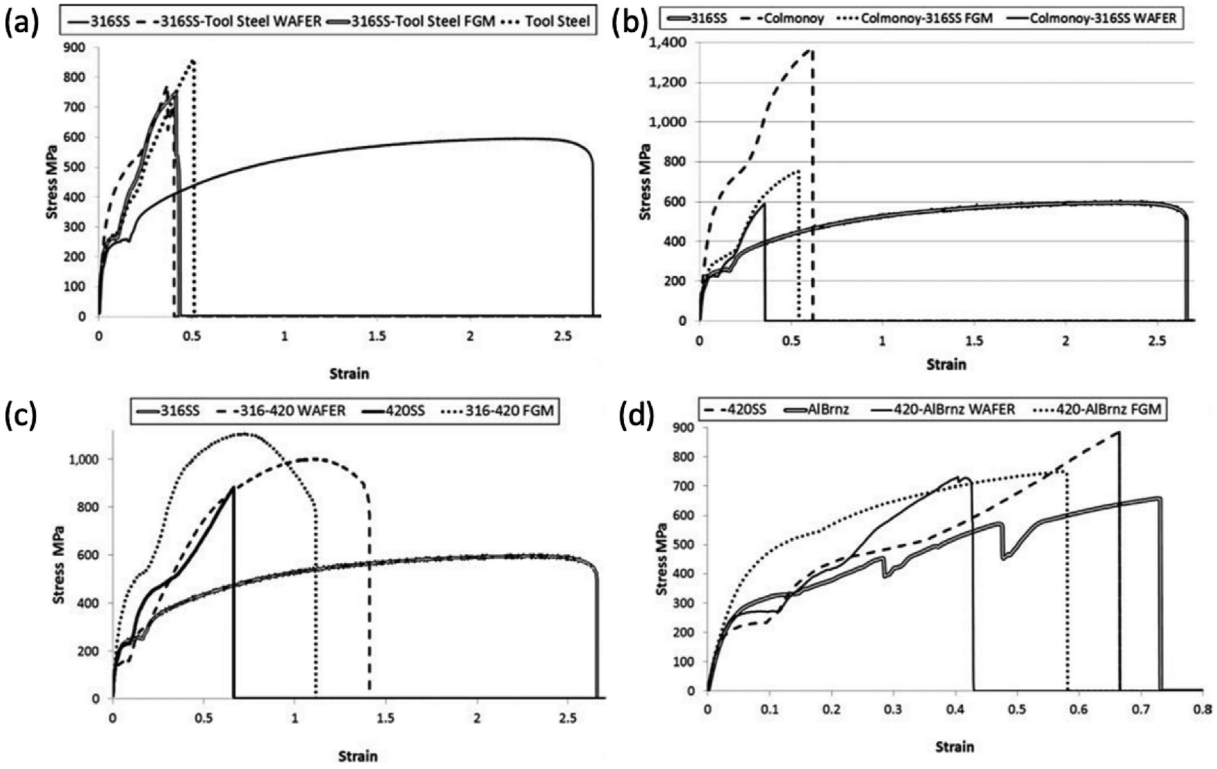

Fig. 24. Stress-strain plot comparisons (a) SS 316L/H13 tool steel, (b) SS 316L/Colmonoy, (c) SS 316L/SS 420 and (d) SS 420/AlBrnz [167].

fluid within a bone implant. The perfusion fluid mechanically stimulates cell proliferation at a given fluid shear stress range. The velocity of fluid flow and shear stress onto the implant surface were calculated in order to evaluate the efficiency of the perfusion fluid within scaffolds of different geometry. Structures with a lower number of layers perpendicular to fluid flow direction are predicted to have better cell attachment, though the longitudinal orientation provide more uniform stress distribution.

Besides the application of FG Ti6Al4V for bone implant scaffolds, the use of Ti metal and FG Ti/TiB composites has also been studied [179]. Han et al. [180] produced five volume fraction combinations (20/5 vol%, 20/7.5 vol%, 20/10 vol%, 20/12.5 vol% and 20/15 vol% Ti) of Schwarts diamond Ti scaffolds by SLM. These volume fraction combinations correspond to 87.93%, 87.17%, 86.94%, 85.08% and 84.03% porosity respectively. The porosities that were measured in actual samples only deviated from the designed porosities by approximately 3.5 vol%. Among these samples, the 20/5 vol% combination has the highest deviation between the designed and the actual porosity because of buckling of its extremely thin struts during manufacturing. Five samples experienced the typical process of elastic deformation, strut fracture and global densification. An oscillation in stress values was observed in four out of five samples, while the 20/12.5 vol% combination is the most pronounced. Each peak in these oscillating stress-strain curve corresponds to plastic deformation of a graded layer. The final rise in stress values indicates a global densification phenomenon after all struts were deformed, and the entire sample becomes a more compact material. A series of real time recordings in Fig. 27 shows the failure process from proximal layer to layers in the middle. The 20/15 vol% sample behaves more like homogeneous porous scaffold and had a significantly higher ultimate strength than other four samples. The graded porosity produces oscillating plateau regions on stress-strain curves corresponding to layer-by-layer fracturing mechanism.

Comparisons between the compressive properties of different FGMs scaffolds are summarized in Table 5.

Table 4
Reported mechanical properties of steel alloy FGMs processed by AM.

Material	AM Technique	Hardness
400W/1000W/400W SS 316L [149]	SLM	Between 150-220HV
SS 316L/Stellite12 with few millimeter transition zone [154]	LDM	From 200HV to 650HV
SS 316L/Stellite12 alternating layers [154]	LDM	Between 300-400HV
SS 316L/Cu bimetallic [155]	SLM	259 ± 7HV - 74 ± 5HV
SS 316L/P21 with 25/50/75% graded layers [82]	DED	From 200HV to 440HV
SS 316L/P21 + 316L SS/P21 [156]	DED	From 210HV to 330HV
SS 316L/NiCr with Cr/Ni ratio varying from 1.4 to 1.7 to 2.3 to 3.7 to 9.7 [157]	LMD	From 1.85 GPa to 6.90 GPa
SS 316L/IN718 bimetallic [158]	EBM	From 148 ± 11HV to 241 ± 12HV
SS 316L/IN718 with 25/50/75% graded layers [159]	LDMD	Between 155.6-186.1HV
SS 410/NiCr/Ti6Al4V [117]	LENS	From 115HV to 275HV
SS 316 L/SS316L + Fe_3Al/Fe_3Al [164]	LENS	From 500HV to 400HV
SS 304 L/IN625 with 1 vol% change per layer [40]	DED	From 210HV to 240HV
Fe–16Cr–8Ni/Fe–14Cr–16Ni/Fe–12Cr–23Ni/Fe–9Cr–28Ni [165]	DED	From 110 HV to 250HV

(SLM: Selective Laser Melting, LDM: Laser-assisted Direct manufacturing, LMD: Laser Metal Deposition, EBM: Energy Beam Melting, LDMD: Laser Direct Metal Deposition, LENS: Laser Energy Net Shaping, DED: Direct Energy Deposition).

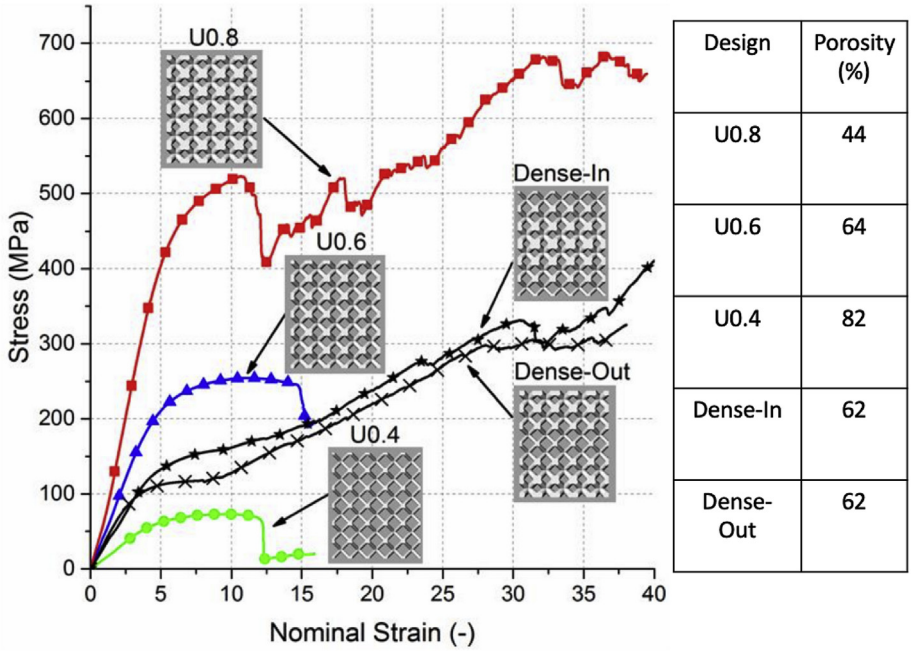

Design	Porosity (%)
U0.8	44
U0.6	64
U0.4	82
Dense-In	62
Dense-Out	62

Fig. 25. Stress-strain comparison between BCC scaffolds with 0.4, 0.6, 0.8 mm diameter and graded dense inward and outward [172].

4.4. Invar 36 alloy

4.4.1. Invar 36/TiC

The use of materials that exhibit a low coefficient of thermal expansion over wide temperature ranges can minimize the internal stress accumulation within AM components. To that effect, Invar 36 (64% Fe and 36% Ni) possesses near zero thermal expansion below 300 °C, which renders it an ideal for AM processing. The low strength is thought to be improved via forming FGMs with TiC and its associated high hardness. Li et al. [181] build an FG Invar 36/TiC composite with 0 vol % to 50 vol% TiC using a 2000 W laser power at a scanning speed of 20 mm/s and a deposition rate of 20 g/min. The addition of TiC effectively modifies the spherical invar grains into dendritic structures as shown in Fig. 28a, and grows more pronounced with increasing TiC as shown from Fig. 28b–f. However, at above 50 vol% TiC, the TiC powder remains unmelted as spherical or faceted grains as shown in Fig. 28f. From Fig. 28g and h, the mechanical properties of Invar 36 are improved, with gradually increasing hardness from 10 HRC to 55 HRC and tensile strength varies from 280 MPa to 500 MPa with increasing vol% of TiC.

4.4.2. Invar 36/V

Bobbio et al. [182] manufactured a FG Invar 36/V composite (shown in Fig. 29a) with varying by 3 vol% within each printed layer from 100 vol% V to 100 vol% Invar 36 using the DED technique. After the 75th layer was printed, the sample fractured entirely around the 30th layer, which prevented the completion of the process. The final macroscopic crack shown in Fig. 29b was caused by small cracks and pores (see Fig. 29d) formed in the region with a composition ranging from 18 to 33 vol% Invar. These cracks can be attributed to the formation of the brittle σ-FeV intermetallic phase. From Fig. 29e and f, thermal dynamic calculations predicted the presence of the σ-FeV intermetallic phase between bcc V and fcc Invar. This prediction was confirmed by the EBSD analysis of 24 vol% to 73 vol% Invar which illustrates the overwhelming σ-FeV from 30 vol% to 58 vol% Invar. As evident that σ-FeV phase drastically increases the hardness to 740-1050HV from 109 to 138HV. In this study, the presence of σ-FeV renders the sample brittle and is likely responsible for the macroscopic crack that formed during fabrication. Through further analysis using computational thermal dynamics, either a non-linear FG compositional change may perhaps be designed to mitigate the negative effect of

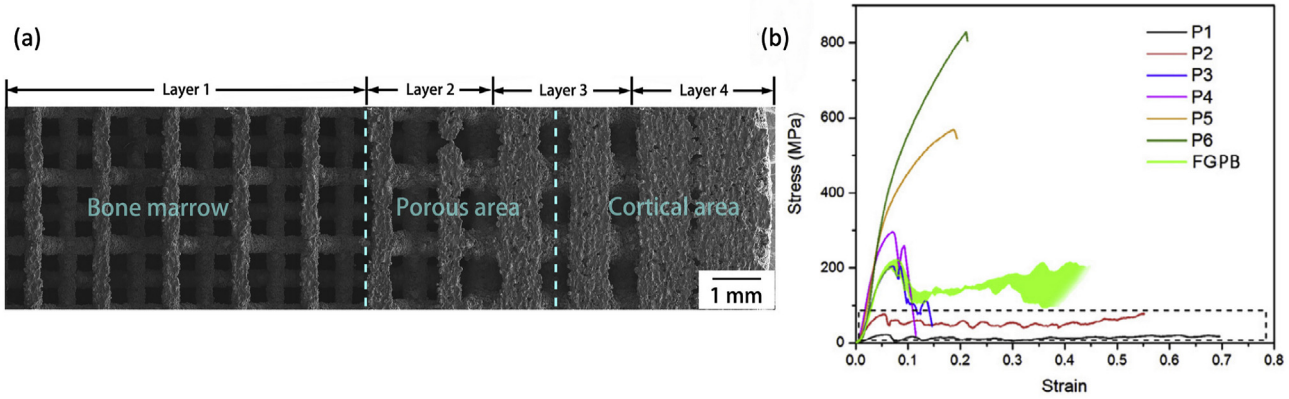

Fig. 26. (a) Lattice structure design representing hierarchical structure of human bone, (b) stress-strain plot comparison among different uniform lattice structures and the four-layerd FGMs structure; P1, P2, P3, P4, P5 and P6 test specimens correspond to 10.5 vol%, 21.0 vol%, 32.6 vol%, 48.4 vol%, 76.9 vol% and 91.3 vol% uniform porosity respectively [177].

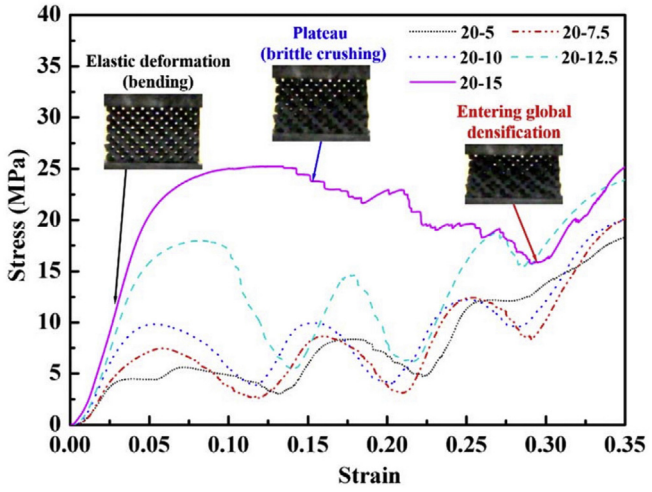

Fig. 27. Deformation process of graded Schwarts diamond Ti scaffold and corresponding stress strain curves showing deformation process and comparison between different porosity combinations [180].

σ-FeV, or alternatively, the high strength of σ-FeV can be deliberately engineered into a component for an appropriate application.

4.5. Other related materials

4.5.1. Al_2O_3

Ceramics are known for their high temperature structural performance, but are often limited to simple geometries due to their poor machinability and low fracture toughness. AM technologies, in principle, can eliminate the concern for geometric limitations, and add fine control to localized microstructure. Though currently, a sintering process needs to take place for additive manufacturing of ceramics either as an investment casting process or a finishing step for printed green bodies. For instance, a FG Al/Al_2O_3 composite were manufactured by Singh et al. [183] through investment casting of FDM prototypes. Al_2O_3 particles in an Al matrix enhances strength, wear and creep resistance with accompanying low weight and thermal expansion. The nylon-Al-Al_2O_3 filaments were first printed and prepared into ceramic molds with molten Al metal poured in afterwards. Some Al_2O_3 particles were found in the Al matrix [184]. Leu et al. [56] fabricated a FG Al_2O_3/ZrO_2 composite that transitions from 50% Al_2O_3 to 75% then 100%. The development of a three-extruder system for freeze-form extrusion fabrication was used to extrude graded ceramic pastes in an environment below 0 °C. The extruded FG Al_2O_3/ZrO_2 composite contained a low binder content, which could be removed through the sintering process. Though the influence of this technique on mechanical performance of the FG ceramics has not been investigated, these innovative approaches highlight the potential for ceramic FGMs.

4.5.2. W/Cu

W has great potential in plasma-facing applications given its marked resistance to neutron damage at high temperatures [185]. Cu can be added onto tungsten as heat sink material for quicker dissipation of heat accumulation [186]. Significant property dissimilarities, such as large melting point and poor solubility, between Cu and W render conventional manufacturing of FG W/Cu composites difficult, while introducing failure-inducing internal stresses [187]. Li et al. [186] used multi-billet extrusion technique to produce a FG W/Cu composite with various compositions ranging from 15 vol%, 25 vol%, 35 vol% Cu. A hydroxypropyl methylcellulose (HPMC) solution was used as a binder for extrusion materials to aid in better bonding of W and Cu. After a sintering post-processing, an FG W/Cu composite with well bonded interfaces and relatively high density were fabricated. However, the liquid state sintering process involved in this technique introduced high strain energy into the crystalline structure, which facilitates the formation of cracks. Tan et al. [188] manufactured bimetallic W/Cu using selective laser melting. Cracks evolved near the bonding region as a result of high residual stress and large thermal expansion mismatch. Interestingly, an inter-diffusion phenomenon can be observed. The opposing surface tension and temperature gradient causes mass transport at the W/Cu interface, which bonds the two materials in the absence of intermetallic phases. This mass transport phenomenon can perhaps be studied in detail and incorporated into the design of novel FG W/Cu composites.

5. Conclusion and future directions

In summary, the objective of this review paper was to introduce the audience to the field of functionally graded materials (FGMs) as related to the emergence of technologies associated with additive manufacturing (AM). It is evident from the vast literature reviewed in this work, that there is increasing interest in the application of AM technologies for the fabrication of FGMs. In a sense, it is the inherent flexibility of AM technologies that render them ideally suited to

Table 5
Mechanical Performance of Porous FGMs processed by AM.

Material (Ti6Al4V)	AM Technique	Mean Porosity (%)	Elastic Modulus (GPa)	Yield Strength (MPa)	Ultimate Compressive Strength (MPa)	Strain (%)
Porous surface with denser core [42]	SLM	37.9	65.1 ± 12.2	578 ± 21	1072 ± 10	26.0 ± 1.0
Porous core with denser surface [42]	SLM	48.4	47.6 ± 11.2	422 ± 14	579 ± 1	18.6 ± 0.1
Gyroid scaffold with linear gradient in density [175]	SLM	25	2.2 ± 0.23	39.8 ± 4.1	43.4 ± 3.5	n/a
Diamond scaffold with linear gradient in density [175]	SLM	25	2.1 ± 0.16	n/a	38.7 ± 2.8	n/a
Gyroid scaffold with gradient cell size [175]	SLM	30	3.8 ± 0.13	126.5 ± 6.2	152.6 ± 4.9	n/a
Diamond scaffold with gradient cell size [175]	SLM	30	3.8 ± 0.26	136.6 ± 5.1	145.7 ± 3.3	n/a
Heterostructure of Gyroid and Diamond [175]	SLM	30	3.6 ± 0.19	n/a	107.5 ± 3.2	n/a
Radially Graded Porous Structure [177]	SLM	59.4	10.44 ± 0.20	170.6 ± 15.6	201.0 ± 10.7	n/a
Diamond 20/5 vol% [180]	SLM	84.99	0.28 ± 0.01	3.7 ± 0.85	n/a	n/a
Diamond 20/7.5 vol% [180]	SLM	84.44	0.33 ± 0.03	4.76 ± 0.13	n/a	n/a
Diamond 20/10 vol% [180]	SLM	83.96	0.38 ± 0.03	6.78 ± 1.03	n/a	n/a
Diamond 20/12.5 vol% [180]	SLM	82.23	0.46 ± 0.02	13.21 ± 0.60	n/a	n/a
Diamond 20/15 vol % [180]	SLM	81.12	0.59 ± 0.02	17.75 ± 0.90	n/a	n/a

(SLM: Selective Laser Melting).

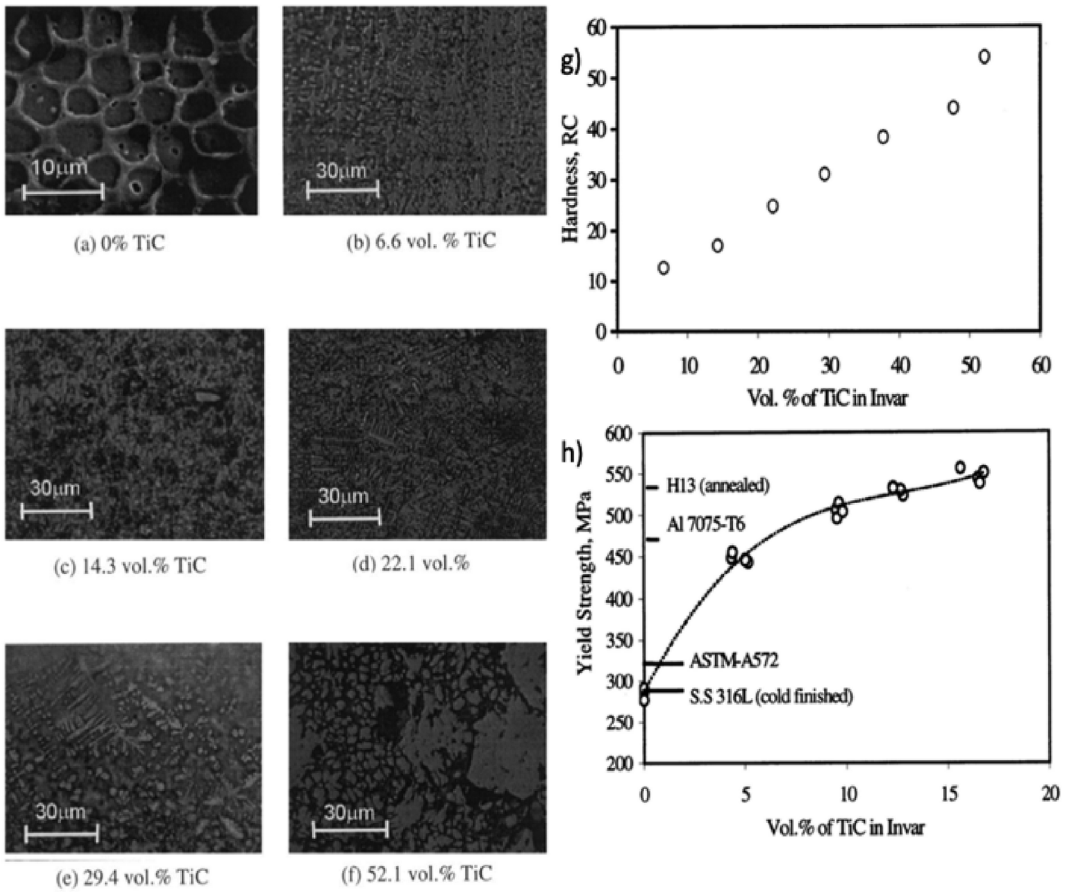

Fig. 28. (a) SEM image of spherical invar grains, (b–e) formation of dendrites with increasing TiC, (f) unmelted TiC powder at above 50 vol% TiC, (g) hardness values with increasing TiC in invar, (h) yield strength at different sections in comparison with other materials [181].

fabricate complex geometries with spatially varying distributions of phases that can be engineered to tailor mechanical and physical properties in a precise way. It is also evident that AM technologies can be used to manufacture an almost infinite combination of alloys, metals, ceramics and composites in very different geometries. It is, however, this precise flexibility that renders AM technologies difficult to develop into reliable commercial products. A number of challenges have emerged that in the view of the authors, must be circumvented and there will be a successful application of AM for the fabrication of FGMs. These are described in details below:

- There are a large number of variables (power density, powder flow rate, displacement velocity, substrate characteristics, etc.) that exert an important influence on a resultant microstructure, phase composition and properties of AM materials. This flexibility also presents an inherent challenge when the need to optimize multiple variables is required in order to attain reproducible properties for a specific material system.
- In terms of optimal alloy design for the successful manufacturing of FGMs using AM technologies, it is also evident that the local and frequently non-equilibrium conditions that are associated with AM, render it hard to predict precise phase composition and microstructure when there are slight variations in the process parameter space. Minor fluctuations in the thermal field, for example can yield changes in microstrucuture.
- Process optimization generally does not carry out from one process to another, making it very difficult to generalize operational principles for the various AM technologies, such as would be required by industry for proper operation of a reliable manufacturing line.

There are however, recent advances and science and technology that promise to help circumvent the above challenges. These are described below:

- First, is the development of artificial intelligence techniques which can potentially help in the design of process and materials that are optimal and can be lead to in-situ optimization of microstructure and properties.
- Second, is the design and implementation of novel diagnostic techniques that when properly arranged with feedback control loops can be used to maintain consistent process conditions. To that effect, there is already some evidence that this strategy is proving to be helpful for AM technologies.
- Third, is the implementation of thermodynamic databases such as CALPHAD, to design alloy compositions a-priori that can then be used in AM to anticipate phase composition and stability.
- Last, is the design and optimization of AM techniques can be used to fabricate multi-dimensional complex multi-functional FGMs that can be applied to extreme working conditions.

In closing, despite the challenges that remain, it is evident that the field of AM and more specifically as applied to FGMs, offers almost unlimited potential. It is clear, however, that there is a large amount of research work that is left to be done.

Acknowledgements

This work was supported by National Key Research and Development Program of China (NO. 2018YFB0905600, and 2017YFB0310400), National Natural Science Foundation of China (No.

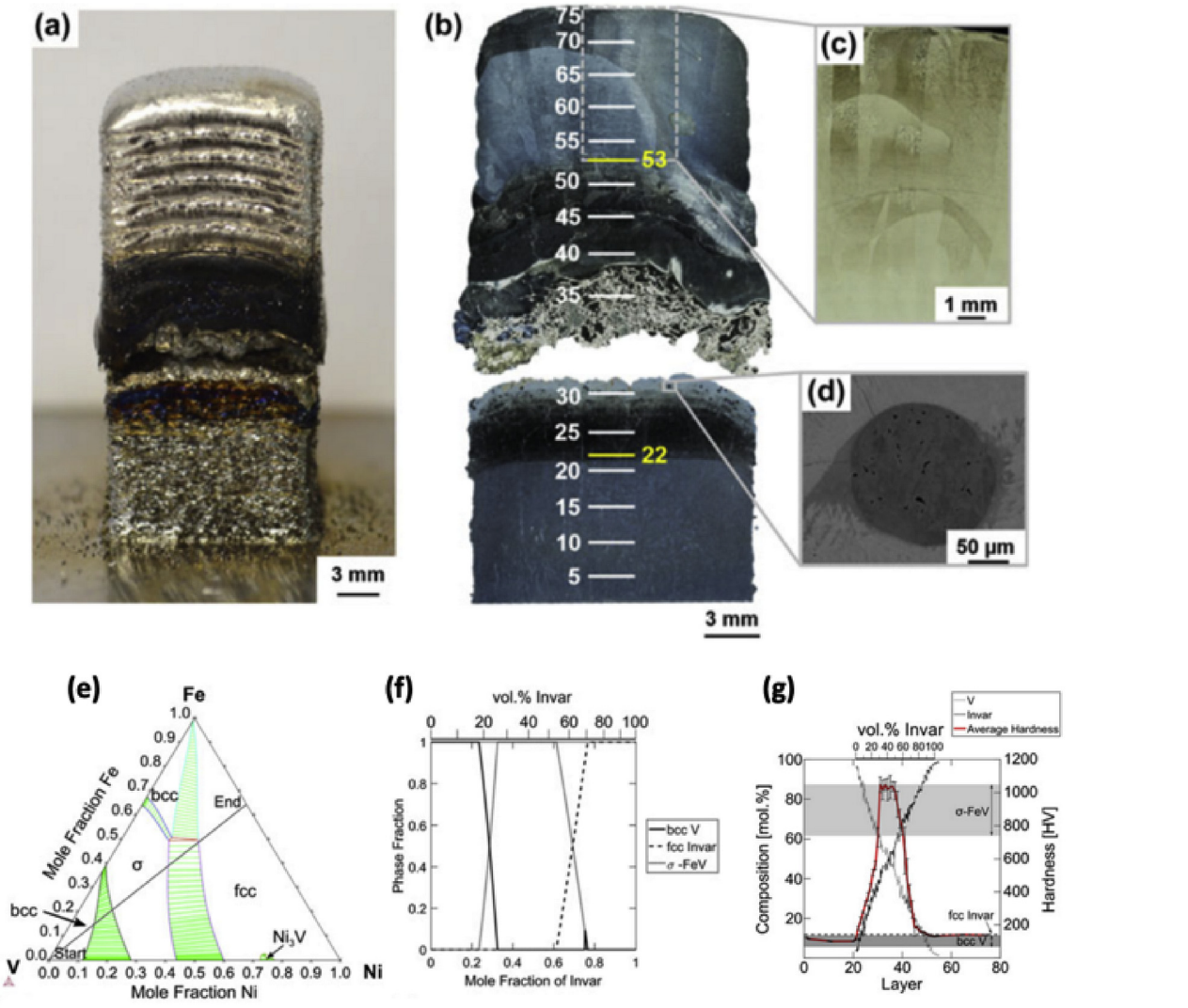

Fig. 29. (a) Photograph of V/Invar sample attached on substrate, (b) cross-section of the cracked sample, (c) elongated grains at 100 vol% Invar, (d) unmelted V particle with pores, (e) ternary diagram of Fe–V–Ni system showing the presence of σ-FeV phase amid V/Invar transition, (f) the computationally predicted dominant σ-FeV phase between pure V and Invar, (g) hardness value increase due to σ-FeV content t [182].

51472188, and 51521001), Natural Research Funds of Hubei Province (No. 2016CFB583), Fundamental Research Funds for the Central Universities China, State Key Laboratory of Advanced Electromagnetic Engineering and Technology (Hua Zhong University of Science and Technology), The Science and Technology Project of Global Energy Interconnection Research Institute Co., Ltd. (SGGR0000WLJS1801080) and the 111 Project (No. B13035).

References

[1] S.S. Wang, Fracture mechanics for delamination problems in composite materials, Stud. Appl. Mech. 6 (3) (1984) 369–383.
[2] N. Noda, Thermal stresses in functionally graded materials, J. Therm. Stress. 22 (4–5) (1999) 477–512.
[3] A.R. Studart, Biological and bioinspired composites with spatially tunable heterogeneous architectures, Adv. Funct. Mater. 23 (36) (2013) 4423–4436.
[4] M. Marc André, M.K. Joanna, C. Po-Yu, Structural biological materials: critical mechanics-materials connections, Science 339 (6121) (2013) 773–779.
[5] P.Y. Chen, J. Mckittrick, M.A. Meyers, Biological materials: functional adaptations and bioinspired designs, Prog. Mater. Sci. 57 (8) (2012) 1492–1704.
[6] F. Barthelat, Y. Zhen, M.J. Buehler, Struct. Mech. Interfaces Biol. Mater. 1 (4) (2016) 16007.
[7] A.R. Studart, Additive manufacturing of biologically-inspired materials, Chem. Soc. Rev. 45 (2) (2016) 359–376.
[8] S.K. Bohidar, R. Sharma, P.R. Mishra, Functionally graded materials: a critical review, Int. J. Res. 1 (4) (2014) 289–301.
[9] G. Knoppers, J. Gunnink, J. Van Den Hout, W. Van Wliet, The Reality of Functionally Graded Material Products, Intelligent Production Machines and Systems-First I* PROMS Virtual Conference: Proceedings and CD-ROM Set, Elsevier, 2005, p. 467.
[10] Z. Liu, M.A. Meyers, Z. Zhang, R.O. Ritchie, Functional gradients and heterogeneities in biological materials: design principles, functions, and bioinspired applications, Prog. Mater. Sci. 88 (2017) 467–498.
[11] K. Pietrzak, D. Kaliński, M. Chmielewski, Interlayer of Al 2 O 3 –Cr functionally graded material for reduction of thermal stresses in alumina–heat resisting steel joints, J. Eur. Ceram. Soc. 27 (2) (2007) 1281–1286.
[12] M. Grujicic, H. Zhao, Optimization of 316 stainless steel/alumina functionally graded material for reduction of damage induced by thermal residual stresses, Mater. Sci. Eng. A 252 (1) (1998) 117–132.
[13] G.H. Loh, E. Pei, D. Harrison, M.D. Monzon, An Overview of Functionally Graded Additive Manufacturing, Additive Manufacturing, (2018).
[14] R.M. Mahamood, E.T. Akinlabi, M. Shukla, S. Pityana, Functionally Graded Material: an Overview, (2012).
[15] M. Naebe, K. Shirvanimoghaddam, Functionally graded materials: a review of fabrication and properties, Appl. Mater. Today 5 (2016) 223–245.
[16] J. Groves, H. Wadley, Functionally graded materials synthesis via low vacuum directed vapor deposition, Compos. B Eng. 28 (1–2) (1997) 57–69.
[17] M. Kawase, T. Tago, M. Kurosawa, H. Utsumi, K. Hashimoto, Chemical vapor infiltration and deposition to produce a silicon carbide–carbon functionally gradient material, Chem. Eng. Sci. 54 (15–16) (1999) 3327–3334.
[18] K. Khor, Y. Gu, Effects of residual stress on the performance of plasma sprayed functionally graded ZrO2/NiCoCrAlY coatings, Mater. Sci. Eng. A 277 (1–2) (2000) 64–76.
[19] S. Stewart, R. Ahmed, T. Itsukaichi, Contact fatigue failure evaluation of post-treated WC–NiCrBSi functionally graded thermal spray coatings, Wear 257 (9–10)

(2004) 962–983.
[20] A. Arsha, E. Jayakumar, T. Rajan, V. Antony, B. Pai, Design and fabrication of functionally graded in-situ aluminium composites for automotive pistons, Mater. Des. 88 (2015) 1201–1209.
[21] B. Kieback, A. Neubrand, H. Riedel, Processing techniques for functionally graded materials, Mater. Sci. Eng. A 362 (1–2) (2003) 81–106.
[22] M.M. Nemat-Alla, M.H. Ata, M.R. Bayoumi, W. Khair-Eldeen, Powder metallurgical fabrication and microstructural investigations of aluminum/steel functionally graded material, Mater. Sci. Appl. 2 (12) (2011) 1708.
[23] P. Samal, J. Newkirk, Powder Metallurgy Methods and Applications vol. 7, ASM Handbook of Powder Metallurgy, 2015.
[24] M. Zhou, J. Xi, J. Yan, Modeling and processing of functionally graded materials for rapid prototyping, J. Mater. Process. Technol. 146 (3) (2004) 396–402.
[25] J. Huang, G.M. Fadel, V.Y. Blouin, M. Grujicic, Bi-objective optimization design of functionally gradient materials, Mater. Des. 23 (7) (2002) 657–666.
[26] A. Pasko, V. Adzhiev, A. Sourin, V. Savchenko, Function representation in geometric modeling: concepts, implementation and applications, Vis. Comput. 11 (8) (1995) 429–446.
[27] W. Chiu, S. Tan, Multiple material objects: from CAD representation to data format for rapid prototyping, Comput. Aided Des. 32 (12) (2000) 707–717.
[28] A.C.F.o.A.M. Technologies, A.C.F.o.A.M.T.S.F.o Terminology, Standard Terminology for Additive Manufacturing Technologies, ASTM International, 2012.
[29] R. Lu, S. Chandrasekaran, W.L. Du Frane, R.L. Landingham, M.A. Worsley, J.D. Kuntz, Complex shaped boron carbides from negative additive manufacturing, Mater. Des. 148 (2018) 8–16.
[30] T.D. Ngo, A. Kashani, G. Imbalzano, K.T. Nguyen, D. Hui, Additive manufacturing (3D printing): a review of materials, methods, applications and challenges, Compos. B Eng. 143 (2018) 172–196.
[31] J.-Y. Lee, J. An, C.K. Chua, Fundamentals and applications of 3D printing for novel materials, Appl. Mater. Today 7 (2017) 120–133.
[32] F. Ning, W. Cong, Microstructures and mechanical properties of Fe-Cr stainless steel parts fabricated by ultrasonic vibration-assisted laser engineered net shaping process, Mater. Lett. 179 (2016) 61–64.
[33] N. Sudarmadji, J. Tan, K. Leong, C. Chua, Y. Loh, Investigation of the mechanical properties and porosity relationships in selective laser-sintered polyhedral for functionally graded scaffolds, Acta Biomater. 7 (2) (2011) 530–537.
[34] K.A. Mumtaz, N. Hopkinson, Laser melting functionally graded composition of Waspaloy® and Zirconia powders, J. Mater. Sci. 42 (18) (2007) 7647–7656.
[35] S. Kumar, S. Pityana, Laser-based Additive Manufacturing of Metals, Advanced Materials Research, Trans Tech Publ, 2011, pp. 92–95.
[36] K.A. Mumtaz, N. Hopkinson, Laser melting functionally graded composition of Waspaloy ® and Zirconia powders, J. Mater. Sci. 42 (18) (2007) 7647–7656.
[37] W. Li, L. Yan, X. Chen, J. Zhang, X. Zhang, F. Liou, Directed energy depositing a new Fe-Cr-Ni alloy with gradually changing composition with elemental powder mixes and particle size'effect in fabrication process, J. Mater. Process. Technol. 255 (2018) 96–104.
[38] Addtive manufacturing, https://www.manufacturingguide.com/en/additiv-tillverkning, (2013) (accessed 8/30.2013).
[39] H.P. Qu, P. Li, S.Q. Zhang, A. Li, H.M. Wang, Microstructure and mechanical property of laser melting deposition (LMD) Ti/TiAl structural gradient material, Mater. Des. 31 (1) (2010) 574–582.
[40] B.E. Carroll, R.A. Otis, J.P. Borgonia, J.-o. Suh, R.P. Dillon, A.A. Shapiro, D.C. Hofmann, Z.-K. Liu, A.M. Beese, Functionally graded material of 304L stainless steel and inconel 625 fabricated by directed energy deposition: characterization and thermodynamic modeling, Acta Mater. 108 (2016) 46–54.
[41] J. del Val, F. Arias-González, O. Barro, A. Riveiro, R. Comesaña, J. Penide, F. Lusquiños, M. Bountinguiza, F. Quintero, J. Pou, Functionally graded 3D structures produced by laser cladding, Procedia Manuf. 13 (2017) 169–176.
[42] S.Y. Choy, C.-N. Sun, K.F. Leong, J. Wei, Compressive properties of functionally graded lattice structures manufactured by selective laser melting, Mater. Des. 131 (2017) 112–120.
[43] M. Fousová, D. Vojtěch, J. Kubásek, E. Jablonská, J. Fojt, Promising characteristics of gradient porosity Ti-6Al-4V alloy prepared by SLM process, J. Mech. Behav. Biomed. Mater. 69 (2017) 368–376.
[44] V. Beal, P. Erasenthiran, N. Hopkinson, P. Dickens, C. Ahrens, The effect of scanning strategy on laser fusion of functionally graded H13/Cu materials, Int. J. Adv. Manuf. Technol. 30 (9–10) (2006) 844–852.
[45] C. Zhou, Y. Chen, Z. Yang, B. Khoshnevis, Digital material fabrication using mask-image-projection-based stereolithography, Rapid Prototyp. J. 19 (3) (2013) 153–165.
[46] S. Kirihara, Additive manufacturing of ceramic components using laser scanning stereolithography, Weld. World 60 (4) (2016) 697–702.
[47] H. Kim, J. Choi, R. Wicker, Process planning and scheduling for multiple material stereolithography, Rapid Prototyp. J. 16 (4) (2010) 232–240.
[48] T. Liu, S. Guessasma, J. Zhu, W. Zhang, S. Belhabib, Functionally graded materials from topology optimisation and stereolithography, Eur. Polym. J. 108 (2018) 199–211.
[49] P. Gonzalez, E. Schwarzer, U. Scheithauer, N. Kooijmans, T. Moritz, Additive manufacturing of functionally graded ceramic materials by stereolithography, JoVE (J. Vis. Exp.) (143) (2019) e57943.
[50] R. Udroiu, I.C. Braga, Polyjet Technology Applications for Rapid Tooling, MATEC Web of Conferences, EDP Sciences, 201703011.
[51] H. Yang, J.C. Lim, Y. Liu, X. Qi, Y.L. Yap, V. Dikshit, W.Y. Yeong, J. Wei, Performance evaluation of projet multi-material jetting 3D printer, Virtual Phys. Prototyp. 12 (1) (2017) 95–103.
[52] Y.L. Yap, C. Wang, S.L. Sing, V. Dikshit, W.Y. Yeong, J. Wei, Material jetting additive manufacturing: an experimental study using designed metrological benchmarks, Precis. Eng. 50 (2017) 275–285.
[53] A. Levy, A. Miriyev, A. Elliott, S.S. Babu, N. Frage, Additive manufacturing of complex-shaped graded TiC/steel composites, Mater. Des. 118 (2017) 198–203.
[54] A. Pandey, S.K. Pradhan, Investigations into complete liquefier dynamics and optimization of process parameters for fused deposition modeling, Mater. Today: Proc. 5 (5) (2018) 12940–12955.
[55] R. Singh, H. Garg, S. Singh, Process capability comparison of fused deposition modelling for ABS and Fe-nylon (6) feedstock filaments, Mater. Today: Proc. 5 (2) (2018) 4258–4268.
[56] M.C. Leu, B.K. Deuser, L. Tang, R.G. Landers, G.E. Hilmas, J.L. Watts, Freeze-form extrusion fabrication of functionally graded materials, CIRP Ann. 61 (1) (2012) 223–226.
[57] N. Singh, R. Singh, I. Ahuja, On development of functionally graded material through fused deposition modelling assisted investment casting from Al 2 O 3/SiC reinforced waste low density polyethylene, Trans. Indian Inst. Met. 71 (10) (2018) 2479–2485.
[58] M. Srivastava, S. Maheshwari, T. Kundra, S. Rathee, R. Yashaswi, S.K. Sharma, Virtual design, modelling and analysis of functionally graded materials by fused deposition modeling, Mater. Today: Proc. 3 (10) (2016) 3660–3665.
[59] S.A. Tofail, E.P. Koumoulos, A. Bandyopadhyay, S. Bose, L. O'Donoghue, C. Charitidis, Additive manufacturing: scientific and technological challenges, market uptake and opportunities, Mater. Today 21 (1) (2018) 22–37.
[60] S. Singh, S. Ramakrishna, R. Singh, Material issues in additive manufacturing: a review, J. Manuf. Process. 25 (2017) 185–200.
[61] Y. Weidong, Optimal Path Planning in Rapid Prototyping Based on Genetic Algorithm, 2009 Chinese Control and Decision Conference, IEEE, 2009, pp. 5068–5072.
[62] N.A. Langrana, D. Qiu, E. Bossett, S.C. Danforth, M. Jafari, A. Safari, Virtual simulation and video microscopy for fused deposition methods, Mater. Des. 21 (2) (2000) 75–82.
[63] D. Qiu, N.A. Langrana, S.C. Danforth, A. Safari, M. Jafari, Intelligent toolpath for extrusion-based LM process, Rapid Prototyp. J. 7 (1) (2001) 18–24.
[64] W. Han, M.A. Jafari, S.C. Danforth, A. Safari, Tool path-based deposition planning in fused deposition processes, J. Manuf. Sci. Eng. 124 (2) (2002) 462–472.
[65] Y.-a. Jin, Y. He, J.-z. Fu, W.-f. Gan, Z.-w. Lin, Optimization of tool-path generation for material extrusion-based additive manufacturing technology, Add. Manuf. 1 (2014) 32–47.
[66] K.-H. Shin, D. Dutta, Constructive representation of heterogeneous objects, J. Comput. Inf. Sci. Eng. 1 (3) (2001) 205–217.
[67] Y. Siu, S. Tan, 'Source-based'heterogeneous solid modeling, Comput. Aided Des. 34 (1) (2002) 41–55.
[68] P. Yang, X. Qian, A B-spline-based approach to heterogeneous objects design and analysis, Comput. Aided Des. 39 (2) (2007) 95–111.
[69] Z. Hongmei, L. Zhigang, L. Bingheng, Heterogeneous object modeling based on multi-color distance field, Mater. Des. 30 (4) (2009) 939–946.
[70] A. Xu, L.L. Shaw, Equal distance offset approach to representing and process planning for solid freeform fabrication of functionally graded materials, Comput. Aided Des. 37 (12) (2005) 1308–1318.
[71] C.C. Wang, Computing on rays: a parallel approach for surface mesh modeling from multi-material volumetric data, Comput. Ind. 62 (7) (2011) 660–671.
[72] X. Qian, D. Dutta, Physics-based modeling for heterogeneous objects, J. Mech. Des. 125 (3) (2003) 416–427.
[73] H.S. Kim, K.-H. Shin, Material pixel-based process planning for layered manufacturing of heterogeneous objects, Int. J. Precis. Eng. Manuf. 15 (11) (2014) 2421–2427.
[74] X. Xiao, S. Joshi, Automatic toolpath generation for heterogeneous objects manufactured by directed energy deposition additive manufacturing process, J. Manuf. Sci. Eng. 140 (7) (2018) 071005.
[75] M. Zhou*, Path planning of functionally graded material objects for layered manufacturing, Int. J. Prod. Res. 42 (2) (2004) 405–415.
[76] P. Muller, P. Mognol, J.-Y. Hascoet, Modeling and control of a direct laser powder deposition process for Functionally Graded Materials (FGM) parts manufacturing, J. Mater. Process. Technol. 213 (5) (2013) 685–692.
[77] P. Muller, J.-Y. Hascoet, P. Mognol, Toolpaths for additive manufacturing of functionally graded materials (FGM) parts, Rapid Prototyp. J. 20 (6) (2014) 511–522.
[78] H. Pohl, A. Simchi, M. Issa, H.C. Dias, Thermal stresses in direct metal laser sintering, Proceedings of the 12th Solid Freeform Fabrication Symposium, Austin, TX, 2001.
[79] N.K. Tolochko, S.E. Mozzharov, I.A. Yadroitsev, T. Laoui, L. Froyen, V.I. Titov, M.B. Ignatiev, Balling processes during selective laser treatment of powders, Rapid Prototyp. J. 10 (2) (2004) 78–87.
[80] J. Jhabvala, E. Boillat, T. Antignac, R. Glardon, On the effect of scanning strategies in the selective laser melting process, Virtual Phys. Prototyp. 5 (2) (2010) 99–109.
[81] S.L. Sing, F.E. Wiria, W.Y. Yeong, Selective laser melting of titanium alloy with 50 wt% tantalum: effect of laser process parameters on part quality, Int. J. Refract. Metals Hard Mater. 77 (2018) 120–127.
[82] W. Woo, D.-K. Kim, E.J. Kingston, V. Luzin, F. Salvemini, M.R. Hill, Effect of interlayers and scanning strategies on through-thickness residual stress distributions in additive manufactured ferritic-austenitic steel structure, Mater. Sci. Eng. A 744 (2019) 618–629.
[83] J. Alcisto, A. Enriquez, H. Garcia, S. Hinkson, T. Steelman, E. Silverman, P. Valdovino, H. Gigerenzer, J. Foyos, J. Ogren, Tensile properties and microstructures of laser-formed Ti-6Al-4V, J. Mater. Eng. Perform. 20 (2) (2011) 203–212.

[84] E. Brandl, B. Baufeld, C. Leyens, R. Gault, Additive manufactured Ti-6Al-4V using welding wire: comparison of laser and are beam deposition and evaluation with respect to aerospace material specifications, Phys. Procedia 5 (2010) 595–606.
[85] A. Ermachenko, R.Y. Lutfullin, R. Mulyukov, Advanced technologies of processing titanium alloys and their applications in industry, Rev. Adv. Mater. Sci. 29 (2011) 68–82.
[86] Y. Hao, J. Liu, J. Li, S. Li, Q. Zou, X. Chen, Rapid preparation of TiC reinforced Ti6Al4V based composites by carburizing method through spark plasma sintering technique, Mater. Des. 65 (2015) 94–97 1980-2015.
[87] Z. Wei, L. Cao, H. Wang, C. Zou, Microstructure and mechanical properties of TiC/Ti–6Al–4V composites processed by in situ casting route, Mater. Sci. Technol. 27 (8) (2011) 1321–1327.
[88] F. Weng, C. Chen, H. Yu, Research status of laser cladding on titanium and its alloys: a review, Mater. Des. 58 (2014) 412–425.
[89] W. Xiang, M. Xuliang, L. Xinlin, D. Lihua, W. Mingjia, Effect of boron addition on microstructure and mechanical properties of TiC/Ti6Al4V composites, Mater. Des. 36 (2012) 41–46 1980-2015.
[90] Y.-J. Kim, H. Chung, S.-J.L. Kang, Processing and mechanical properties of Ti–6Al–4V/TiC in situ composite fabricated by gas–solid reaction, Mater. Sci. Eng. A 333 (1–2) (2002) 343–350.
[91] J. Zhu, P. Liaw, J. Corum, H. McCoy, High-temperature mechanical behavior of Ti-6Al-4V alloy and TiC p/Ti-6Al-4V composite, Metall. Mater. Trans. A 30 (6) (1999) 1569–1578.
[92] H. Choe, S. Abkowitz, S.M. Abkowitz, D.C. Dunand, Mechanical properties of Ti–W alloys reinforced with TiC particles, Mater. Sci. Eng. A 485 (1–2) (2008) 703–710.
[93] L. Li, J. Wang, P. Lin, H. Liu, Microstructure and mechanical properties of functionally graded TiCp/Ti6Al4V composite fabricated by laser melting deposition, Ceram. Int. 43 (18) (2017) 16638–16651.
[94] F. Wang, J. Mei, X. Wu, Compositionally graded Ti6Al4V+ TiC made by direct laser fabrication using powder and wire, Mater. Des. 28 (7) (2007) 2040–2046.
[95] J. Obielodan, B. Stucker, Characterization of LENS-fabricated Ti6Al4V and Ti6Al4V/TiC dual-material transition joints, Int. J. Adv. Manuf. Technol. 66 (9–12) (2013) 2053–2061.
[96] D. Liu, S. Zhang, A. Li, H. Wang, Microstructure and tensile properties of laser melting deposited TiC/TA15 titanium matrix composites, J. Alloy. Comp. 485 (1–2) (2009) 156–162.
[97] J. Zhang, Y. Zhang, W. Li, S. Karnati, F. Liou, J.W. Newkirk, Microstructure and properties of functionally graded materials ti6al4v/tic fabricated by direct laser deposition, Rapid Prototyp. J. 24 (4) (2018) 677–687.
[98] O. Ochonogor, C. Meacock, M. Abdulwahab, S. Pityana, Effects of Ti and TiC ceramic powder on laser-cladded Ti–6Al–4V in situ intermetallic composite, Appl. Surf. Sci. 263 (2012) 591–596.
[99] K.I. Schwendner, R. Banerjee, P.C. Collins, C.A. Brice, H.L. Fraser, Direct laser deposition of alloys from elemental powder blends, Scr. Mater. 45 (10) (2001) 1123–1129.
[100] H. Rastegari, S. Asgari, S. Abbasi, Producing Ti–6Al–4V/TiC composite with good ductility by vacuum induction melting furnace and hot rolling process, Mater. Des. 32 (10) (2011) 5010–5014.
[101] Y. Lu, H. Tang, Y. Fang, D. Liu, H. Wang, Microstructure evolution of sub-critical annealed laser deposited Ti–6Al–4V alloy, Mater. Des. 37 (2012) 56–63.
[102] R.M. Mahamood, E.T. Akinlabi, M. Shukla, S. Pityana, Characterization of Laser Deposited Ti6Al4V/TiC Composite Powders on a Ti6Al4V Substrate, (2014).
[103] R.M. Mahamood, E.T. Akinlabi, M. Shukla, S. Pityana, Scanning velocity influence on microstructure, microhardness and wear resistance performance of laser deposited Ti6Al4V/TiC composite, Mater. Des. 50 (2013) 656–666.
[104] R. Mahamood, E.T. Akinlabi, Laser metal deposition of functionally graded Ti6Al4V/TiC, Mater. Des. 84 (2015) 402–410.
[105] R.M. Mahamood, E.T. Akinlabi, Modelling of Process Parameters Influence on Degree of Porosity in Laser Metal Deposition Process, Transactions on Engineering Technologies, Springer, 2015, pp. 31–42.
[106] R.M. Mahamood, E.T. Akinlabi, Effect of laser power and powder flow rate on the wear resistance behaviour of laser metal deposited TiC/Ti6Al4 V composites, Mater. Today: Proc. 2 (4–5) (2015) 2679–2686.
[107] R.M. Mahamood, E.T. Akinlabi, Scanning speed and powder flow rate influence on the properties of laser metal deposition of titanium alloy, Int. J. Adv. Manuf. Technol. 91 (5–8) (2017) 2419–2426.
[108] J. Wang, L. Li, P. Lin, J. Wang, Effect of TiC particle size on the microstructure and tensile properties of TiCp/Ti6Al4V composites fabricated by laser melting deposition, Opt. Laser. Technol. 105 (2018) 195–206.
[109] J.-B. Fruhauf, J. Roger, O. Dezellus, S. Gourdet, N. Karnatak, N. Peillon, S. Saunier, F. Montheillet, C. Desrayaud, Microstructural and mechanical comparison of Ti+15% TiCp composites prepared by free sintering, HIP and extrusion, Mater. Sci. Eng. A 554 (2012) 22–32.
[110] D. Gu, Y.-C. Hagedorn, W. Meiners, K. Wissenbach, R. Poprawe, Nanocrystalline TiC reinforced Ti matrix bulk-form nanocomposites by Selective Laser Melting (SLM): densification, growth mechanism and wear behavior, Compos. Sci. Technol. 71 (13) (2011) 1612–1620.
[111] S. Liu, Y.C. Shin, The influences of melting degree of TiC reinforcements on microstructure and mechanical properties of laser direct deposited Ti6Al4V-TiC composites, Mater. Des. 136 (2017) 185–195.
[112] F. Wang, J. Mei, X. Wu, Direct laser fabrication of Ti6Al4V/TiB, J. Mater. Process. Technol. 195 (1–3) (2008) 321–326.
[113] D. Gu, W. Meiners, K. Wissenbach, R. Poprawe, Laser additive manufacturing of metallic components: materials, processes and mechanisms, Int. Mater. Rev. 57 (3) (2012) 133–164.
[114] U.K. Mudali, B.A. Rao, K. Shanmugam, R. Natarajan, B. Raj, Corrosion and microstructural aspects of dissimilar joints of titanium and type 304L stainless steel, J. Nucl. Mater. 321 (1) (2003) 40–48.
[115] H. Dey, M. Ashfaq, A. Bhaduri, K.P. Rao, Joining of titanium to 304L stainless steel by friction welding, J. Mater. Process. Technol. 209 (18–19) (2009) 5862–5870.
[116] S. Kundu, S. Sam, S. Chatterjee, Evaluation of interface microstructure and mechanical properties of the diffusion bonded joints of Ti–6Al–4V alloy to micro-duplex stainless steel, Mater. Sci. Eng. A 528 (15) (2011) 4910–4916.
[117] H. Sahasrabudhe, R. Harrison, C. Carpenter, A. Bandyopadhyay, Stainless steel to titanium bimetallic structure using LENS™, Addit. Manuf. 5 (2015) 1–8.
[118] B. Onuike, A. Bandyopadhyay, Additive manufacturing of Inconel 718–Ti6Al4V bimetallic structures, Addit. Manuf. 22 (2018) 844–851.
[119] I. Tomashchuk, D. Grevey, P. Sallamand, Dissimilar laser welding of AISI 316L stainless steel to Ti6–Al4–6V alloy via pure vanadium interlayer, Mater. Sci. Eng. A 622 (2015) 37–45.
[120] I. Tomashchuk, P. Sallamand, N. Belyavina, M. Pilloz, Evolution of microstructures and mechanical properties during dissimilar electron beam welding of titanium alloy to stainless steel via copper interlayer, Mater. Sci. Eng. A 585 (2013) 114–122.
[121] S. Kundu, M. Ghosh, A. Laik, K. Bhanumurthy, G. Kale, S. Chatterjee, Diffusion bonding of commercially pure titanium to 304 stainless steel using copper interlayer, Mater. Sci. Eng. A 407 (1–2) (2005) 154–160.
[122] S. Kundu, S. Chatterjee, Characterization of diffusion bonded joint between titanium and 304 stainless steel using a Ni interlayer, Mater. Char. 59 (5) (2008) 631–637.
[123] P. He, X. Yue, J. Zhang, Hot pressing diffusion bonding of a titanium alloy to a stainless steel with an aluminum alloy interlayer, Mater. Sci. Eng. A 486 (1–2) (2008) 171–176.
[124] M. Lee, J. Lee, Y. Choi, D. Kim, C. Rhee, Y. Lee, S. Hong, Interlayer engineering for dissimilar bonding of titanium to stainless steel, Mater. Lett. 64 (9) (2010) 1105–1108.
[125] L.D. Bobbio, B. Bocklund, R. Otis, J.P. Borgonia, R.P. Dillon, A.A. Shapiro, B. McEnerney, Z.-K. Liu, A.M. Beese, Characterization of a functionally graded material of Ti-6Al-4V to 304L stainless steel with an intermediate V section, J. Alloy. Comp. 742 (2018) 1031–1036.
[126] N. Saunders, A.P. Miodownik, CALPHAD (Calculation of Phase Diagrams): a Comprehensive Guide, Elsevier, 1998.
[127] H. Lukas, S.G. Fries, B. Sundman, Computational Thermodynamics: the Calphad Method, Cambridge university press, 2007.
[128] Z.-K. Liu, First-principles calculations and CALPHAD modeling of thermodynamics, J. Phase Equilibria Diffusion 30 (5) (2009) 517.
[129] Z.-K. Liu, Design Magnesium Alloys: How Computational Thermodynamics Can Help, Essential Readings in Magnesium Technology, Springer, 2016, pp. 403–410.
[130] A. Reichardt, R.P. Dillon, J.P. Borgonia, A.A. Shapiro, B.W. McEnerney, T. Momose, P. Hosemann, Development and characterization of Ti-6Al-4V to 304L stainless steel gradient components fabricated with laser deposition additive manufacturing, Mater. Des. 104 (2016) 404–413.
[131] W. Li, S. Karnati, C. Kriewall, F. Liou, J. Newkirk, K.M.B. Taminger, W.J. Seufzer, Fabrication and characterization of a functionally graded material from Ti-6Al-4V to SS316 by laser metal deposition, Addit. Manuf. 14 (2017) 95–104.
[132] L.D. Bobbio, R.A. Otis, J.P. Borgonia, R.P. Dillon, A.A. Shapiro, Z.-K. Liu, A.M. Beese, Additive manufacturing of a functionally graded material from Ti-6Al-4V to Invar: experimental characterization and thermodynamic calculations, Acta Mater. 127 (2017) 133–142.
[133] J. De Keyzer, G. Cacciamani, N. Dupin, P. Wollants, Thermodynamic modeling and optimization of the Fe–Ni–Ti system, Calphad 33 (1) (2009) 109–123.
[134] M. Ghosh, S. Chatterjee, B. Mishra, The effect of intermetallics on the strength properties of diffusion bonds formed between Ti–5.5 Al–2.4 V and 304 stainless steel, Mater. Sci. Eng. A 363 (1–2) (2003) 268–274.
[135] C. Schneider-Maunoury, L. Weiss, P. Acquier, D. Boisselier, P. Laheurte, Functionally graded Ti6Al4V-Mo alloy manufactured with DED-CLAD® process, Addit. Manuf. 17 (2017) 55–66.
[136] Z. Yang, X. Zheng, W. Cai, Martensitic transformation and shape memory effect of Ti–V–Al lightweight high-temperature shape memory alloys, Scr. Mater. 99 (2015) 97–100.
[137] X. Chen, J. Yan, S. Ren, J. Wei, Q. Wang, Microstructure and mechanical properties of Ti–6Al–4V/Al1060 joints by ultrasonic-assisted brazing in air, Mater. Lett. 95 (2013) 197–200.
[138] Y. Zhang, A. Bandyopadhyay, Direct fabrication of compositionally graded Ti-Al2O3 multi-material structures using Laser Engineered Net Shaping, Addit. Manuf. 21 (2018) 104–111.
[139] F. Niu, D. Wu, S. Yan, G. Ma, B. Zhang, Process optimization for suppressing cracks in laser engineered net shaping of Al 2 O 3 ceramics, JOM 69 (3) (2017) 557–562.
[140] S. Yin, X. Yan, C. Chen, R. Jenkins, M. Liu, R. Lupoi, Hybrid additive manufacturing of Al-Ti6Al4V functionally graded materials with selective laser melting and cold spraying, J. Mater. Process. Technol. 255 (2018) 650–655.
[141] N. Baddoo, Stainless steel in construction: a review of research, applications, challenges and opportunities, J. Constr. Steel Res. 64 (11) (2008) 1199–1206.
[142] S. Heuer, J. Matějíček, M. Vilémová, M. Koller, K. Illkova, J. Veverka, T. Weber, G. Pintsuk, J. Coenen, C. Linsmeier, Atmospheric Plasma Spraying of Functionally Graded Steel/tungsten Layers for the First Wall of Future Fusion Reactors, Surface and Coatings Technology, 2019.
[143] M. Dourandish, A. Simchi, K. Hokamoto, S. Tanaka, Phase formation during sintering of nanocrystalline zirconia/stainless steel functionally graded composite layers, Mater. Lett. 65 (3) (2011) 523–526.
[144] L. Thijs, K. Kempen, J.-P. Kruth, J. Van Humbeeck, Fine-structured aluminium products with controllable texture by selective laser melting of pre-alloyed

AlSi10Mg powder, Acta Mater. 61 (5) (2013) 1809–1819.
[145] K. Amato, S. Gaytan, L. Murr, E. Martinez, P. Shindo, J. Hernandez, S. Collins, F. Medina, Microstructures and mechanical behavior of Inconel 718 fabricated by selective laser melting, Acta Mater. 60 (5) (2012) 2229–2239.
[146] L. Thijs, M.L.M. Sistiaga, R. Wauthle, Q. Xie, J.-P. Kruth, J. Van Humbeeck, Strong morphological and crystallographic texture and resulting yield strength anisotropy in selective laser melted tantalum, Acta Mater. 61 (12) (2013) 4657–4668.
[147] T. Amine, J.W. Newkirk, F. Liou, An investigation of the effect of laser deposition parameters on characteristics of multilayered 316 L deposits, Int. J. Adv. Manuf. Technol. 73 (9–12) (2014) 1739–1749.
[148] T. Niendorf, S. Leuders, A. Riemer, H.A. Richard, T. Tröster, D. Schwarze, Highly anisotropic steel processed by selective laser melting, Metall. Mater. Trans. B 44 (4) (2013) 794–796.
[149] T. Niendorf, S. Leuders, A. Riemer, F. Brenne, T. Tröster, H.A. Richard, D. Schwarze, Functionally graded alloys obtained by additive manufacturing, Adv. Eng. Mater. 16 (7) (2014) 857–861.
[150] A. Khoddamzadeh, R. Liu, M. Liang, Q. Yang, Novel wear-resistant materials–Carbon fiber reinforced low-carbon Stellite alloy composites, Compos. Appl. Sci. Manuf. 43 (3) (2012) 344–352.
[151] J. Yao, Y. Ding, R. Liu, Q. Zhang, L. Wang, Wear and corrosion performance of laser-clad low-carbon high-molybdenum Stellite alloys, Opt. Laser. Technol. 107 (2018) 32–45.
[152] G. Lucchetta, R. Giusti, S. Vezzù, P. Bariani, Investigation and characterization of Stellite-based wear-resistant coatings applied to steel moulds by cold-spray, CIRP Ann. 64 (1) (2015) 535–538.
[153] M.M. Ferozhkhan, K.G. Kumar, R. Ravibharath, Metallurgical study of stellite 6 cladding on 309-16l stainless steel, Arabian J. Sci. Eng. 42 (5) (2017) 2067–2074.
[154] A. Yakovlev, E. Trunova, D. Grevey, M. Pilloz, I. Smurov, Laser-assisted direct manufacturing of functionally graded 3D objects, Surf. Coat. Technol. 190 (1) (2005) 15–24.
[155] Z. Liu, D. Zhang, S. Sing, C. Chua, L. Loh, Interfacial characterization of SLM parts in multi-material processing: metallurgical diffusion between 316L stainless steel and C18400 copper alloy, Mater. Char. 94 (2014) 116–125.
[156] D.-K. Kim, W. Woo, E.-Y. Kim, S.-H. Choi, Microstructure and mechanical characteristics of multi-layered materials composed of 316L stainless steel and ferritic steel produced by direct energy deposition, J. Alloy. Comp. 774 (2019) 896–907.
[157] C. Zhang, H. Zhang, C. Wu, S. Zhang, Z. Sun, S. Dong, Multi-layer functional graded stainless steel fabricated by laser melting deposition, Vacuum 141 (2017) 181–187.
[158] A. Hinojos, J. Mireles, A. Reichardt, P. Frigola, P. Hosemann, L.E. Murr, R.B. Wicker, Joining of Inconel 718 and 316 Stainless Steel using electron beam melting additive manufacturing technology, Mater. Des. 94 (2016) 17–27.
[159] K. Shah, I. ul Haq, A. Khan, S.A. Shah, M. Khan, A.J. Pinkerton, Parametric study of development of Inconel-steel functionally graded materials by laser direct metal deposition, Mater. Des. 54 (2014) 531–538 1980-2015.
[160] J. Strößner, M. Terock, U. Glatzel, Mechanical and microstructural investigation of nickel-based superalloy IN718 manufactured by selective laser melting (SLM), Adv. Eng. Mater. 17 (8) (2015) 1099–1105.
[161] Y. Chen, H. Wang, Microstructure and wear resistance of laser clad TiC reinforced FeAl intermetallic matrix composite coatings, Surf. Coat. Technol. 168 (1) (2003) 30–36.
[162] S.-c. Wei, B.-s. Xu, H.-d. Wang, G. Jin, H. Lv, Comparison on corrosion-resistance performance of electro-thermal explosion plasma spraying FeAl-based coatings, Surf. Coat. Technol. 201 (9–11) (2007) 5294–5297.
[163] S. Ghosh, V.P.S. Rana, V. Kain, V. Mittal, S. Baveja, Role of residual stresses induced by industrial fabrication on stress corrosion cracking susceptibility of austenitic stainless steel, Mater. Des. 32 (7) (2011) 3823–3831.
[164] T. Durejko, M. Ziętala, W. Polkowski, T. Czujko, Thin wall tubes with Fe3Al/SS316L graded structure obtained by using laser engineered net shaping technology, Mater. Des. 63 (2014) 766–774.
[165] W. Li, X. Chen, L. Yan, J. Zhang, X. Zhang, F. Liou, Additive manufacturing of a new Fe-Cr-Ni alloy with gradually changing compositions with elemental powder mixes and thermodynamic calculation, Int. J. Adv. Manuf. Technol. 95 (1–4) (2018) 1013–1023.
[166] M. Soodi, S. Masood, M. Brandt, Thermal expansion of functionally graded and wafer-layered structures produced by laser direct metal deposition, Int. J. Adv. Manuf. Technol. 69 (9–12) (2013) 2011–2018.
[167] M. Soodi, S.H. Masood, M. Brandt, Tensile strength of functionally graded and wafer layered structures produced by direct metal deposition, Rapid Prototyp. J. 20 (5) (2014) 360–368.
[168] R. Huiskes, H. Weinans, B. Van Rietbergen, The relationship between stress shielding and bone resorption around total hip stems and the effects of flexible materials, Clin. Orthop. Relat. Res. (1992) 124–134.
[169] D. Mahmoud, M. Elbestawi, Lattice structures and functionally graded materials applications in additive manufacturing of orthopedic implants: a review, J. Manuf. Mater. Proc. 1 (2) (2017) 13.
[170] R. Bothe, Reaction of bone to multiple metallic implants, Surg. Gynecol. Obstet. 71 (1940) 598–602.
[171] Y. Torres, P. Trueba, J. Pavón, E. Chicardi, P. Kamm, F. García-Moreno, J. Rodríguez-Ortiz, Design, processing and characterization of titanium with radial graded porosity for bone implants, Mater. Des. 110 (2016) 179–187.
[172] E. Onal, J. Frith, M. Jurg, X. Wu, A. Molotnikov, Mechanical properties and in vitro behavior of additively manufactured and functionally graded Ti6Al4V porous scaffolds, Metals 8 (4) (2018) 200.
[173] J.P. Li, P. Habibovic, M. van den Doel, C.E. Wilson, J.R. de Wijn, C.A. van Blitterswijk, K. de Groot, Bone ingrowth in porous titanium implants produced by 3D fiber deposition, Biomaterials 28 (18) (2007) 2810–2820.
[174] M.-T. Hsieh, B. Endo, Y. Zhang, J. Bauer, L. Valdevit, The mechanical response of cellular materials with spinodal topologies, J. Mech. Phys. Solids 125 (2019) 401–419.
[175] F. Liu, Z. Mao, P. Zhang, D.Z. Zhang, J. Jiang, Z. Ma, Functionally graded porous scaffolds in multiple patterns: new design method, physical and mechanical properties, Mater. Des. 160 (2018) 849–860.
[176] L. Xiao, W. Song, Additively-manufactured functionally graded Ti-6Al-4V lattice structures with high strength under static and dynamic loading: Experiments, Int. J. Impact Eng. 111 (2018) 255–272.
[177] X.-Y. Zhang, G. Fang, S. Leeflang, A.A. Zadpoor, J. Zhou, Topological design, permeability and mechanical behavior of additively manufactured functionally graded porous metallic biomaterials, Acta Biomater. 84 (2019) 437–452.
[178] A.L. Olivares, È. Marsal, J.A. Planell, D. Lacroix, Finite element study of scaffold architecture design and culture conditions for tissue engineering, Biomaterials 30 (30) (2009) 6142–6149.
[179] H. Attar, L. Löber, A. Funk, M. Calin, L. Zhang, K. Prashanth, S. Scudino, Y. Zhang, J. Eckert, Mechanical behavior of porous commercially pure Ti and Ti–TiB composite materials manufactured by selective laser melting, Mater. Sci. Eng. A 625 (2015) 350–356.
[180] C. Han, Y. Li, Q. Wang, S. Wen, Q. Wei, C. Yan, L. Hao, J. Liu, Y. Shi, Continuous functionally graded porous titanium scaffolds manufactured by selective laser melting for bone implants, J. Mech. Behav. Biomed. Mater. 80 (2018) 119–127.
[181] X.C. Li, J. Stampfl, F.B. Prinz, Mechanical and thermal expansion behavior of laser deposited metal matrix composites of Invar and TiC, Mater. Sci. Eng. A 282 (1–2) (2000) 86–90.
[182] L.D. Bobbio, B. Bocklund, R. Otis, J.P. Borgonia, R.P. Dillon, A.A. Shapiro, B. McEnerney, Z.-K. Liu, A.M. Beese, Experimental analysis and thermodynamic calculations of an additively manufactured functionally graded material of V to Invar 36, J. Mater. Res. 33 (11) (2018) 1642–1649.
[183] S. Singh, R. Singh, Wear modelling of Al-Al2O3 functionally graded material prepared by FDM assisted investment castings using dimensionless analysis, J. Manuf. Process. 20 (2015) 507–514.
[184] S.A. Sajjadi, H. Ezatpour, H. Beygi, Microstructure and mechanical properties of Al–Al2O3 micro and nano composites fabricated by stir casting, Mater. Sci. Eng. A 528 (29–30) (2011) 8765–8771.
[185] H. Bolt, V. Barabash, W. Krauss, J. Linke, R. Neu, S. Suzuki, N. Yoshida, A.U. Team, Materials for the plasma-facing components of fusion reactors, J. Nucl. Mater. 329 (2004) 66–73.
[186] S.-B. Li, J.-X. Xie, Processing and microstructure of functionally graded W/Cu composites fabricated by multi-billet extrusion using mechanically alloyed powders, Compos. Sci. Technol. 66 (13) (2006) 2329–2336.
[187] X. Tang, H. Zhang, D. Du, D. Qu, C. Hu, R. Xie, Y. Feng, Fabrication of W–Cu functionally graded material by spark plasma sintering method, Int. J. Refract. Metals Hard Mater. 42 (2014) 193–199.
[188] C. Tan, K. Zhou, T. Kuang, Selective laser melting of tungsten-copper functionally graded material, Mater. Lett. 237 (2019) 328–331.